Highlights

A Microgrid Control Scheme for Islanded Operation and Re-synchronization utilizing Model Predictive Control

Fernando Fachini, Tetiana Bogodorova, Luigi Vanfretti, Sjoerd Boersma

- *Highlight 1* - A Modelica-based microgrid dynamic model for control and optimization studies.
- *Highlight 2* - A Model Predictive Control (MPC) framework combining Modelica models, Dymola and MATLAB software.
- *Highlight 3* - An MPC-based secondary frequency control scheme for islanded microgrids.
- *Highlight 4* - An MPC-based re-synchronization control scheme applicable to microgrids or distributed generation resources.
- *Highlight 5* - Comparison of the proposed MPC-based schemes against state-of-the-art controllers.

A Microgrid Control Scheme for Islanded Operation and Re-synchronization utilizing Model Predictive Control

Fernando Fachini[a], Tetiana Bogodorova[a], Luigi Vanfretti[a], Sjoerd Boersma[b]

[a] *Rensselaer Polytechnic Institute, Department of Electrical, Computer, and Systems Engineering, 110 8th St, Troy, NY, 12180, United States*
[b] *Wageningen University & Research, Wageningen Plant Research, Biometris, Droevendaalsesteeg 1, 6708 PB, Wageningen, The Netherlands*

Abstract

Enhancing grid resilience is proposed through the integration of distributed energy resources (DERs) with microgrids. Due to the diverse nature of DERs, there is a need to explore the optimal combined operation of these energy sources within the framework of microgrids. As such, this paper presents the design, implementation and validation of a Model Predictive Control (MPC)-based secondary control scheme to tackle two challenges: optimal islanded operation, and optimal re-synchronization of a microgrid. The MPC optimization algorithm dynamically adjusts input signals, termed manipulated variables, for each DER within the microgrid, including a gas turbine, an aggregate photovoltaic (PV) unit, and an electrical battery energy storage (BESS) unit. To attain optimal islanded operation, the secondary-level controller based on Model Predictive Control (MPC) was configured to uphold microgrid functionality promptly following the islanding event. Subsequently, it assumed the task of power balancing within the microgrid and ensuring the reliability of the overall system. For optimal re-synchronization, the MPC-based controller was set to adjust the manipulated variables to synchronize voltage and angle with the point of common coupling of the system. All stages within the microgrid operation were optimally achieved through one MPC-driven control system, where the controller can effectively guide the system to different goals by updating the MPC's target reference. More importantly, the results show that the MPC-based control scheme is capable of controlling different DERs simultaneously, mitigating potentially harmful transient rotor torques from the re-synchronization as well as maintaining the microgrid within system performance requirements.

Keywords: Microgrid, Model Predictive Control, Optimization, Secondary-level control, Re-synchronization, Islanding, OpenIPSL, Modelica

1. Introduction

1.1. Motivation

Traditional power systems rely on large centralized plants, historically placed near natural resources, to generate electricity for consumption (1; 2). However, a shift towards alternative structures, emphasizing Distributed Energy Resources (DERs) like microgrids, is gaining traction. Microgrids, small and intentionally delimited electrical grids, enhance system reliability and resilience (3). Recognizing microgrids as a "key building block for a Smart Grid," the U.S. Department of Energy supports research to accelerate their development (4). Successful microgrid projects have notably improved reliability in various small-scale facilities, such as military bases (5), hospitals (6), data centers (7), residential neighborhoods (8), university campuses (9), and industrial plants (10). Improved reliability is exemplified through operation reserves and ancillary services, utilizing power electronic-based sources like Battery Energy Storage Systems (BESS) and photovoltaic (PV) systems (11).

Because of the capability of operating in both grid-connected and islanded modes, the microgrid must be able to transition from one operational mode to another in the most seamless way possible (12) in order to mitigate transients during the islanding (13) and re-synchronization stages (14). Reactive power control of inverter-based resources can support system voltages, while batteries can aid in frequency support (15). In addition to that, batteries can also help with long-term ancillary services, such as power smoothing and load following (11).

Currently, microgrids use a hierarchical control structure similar to that of the bulk power system, which is divided into three stages: primary, secondary, and tertiary level controls (16). However, even when microgrids meet the requirements to operate autonomously (17), islanding and re-synchronization controls need to be in place to facilitate their transition between autonomous and grid-connected operating modes. Existing methodologies could be deployed to achieve this goal, but studies have shown that it is challenging to design adequate control settings (18), and also to limit the torsional impact of DERs in the microgrid (19). This implies that alternative methods might be attractive to address these and other potential limitations.

In this work, we investigate an alternative hierarchical control approach that exploits Model Predictive Control (MPC) and may offer a compelling option to optimally operate microgrids through the aforementioned transitions. Additionally, MPC for microgrid applications is currently in its early developmental phase, and is expected to emerge as a competitive alternative to conventional microgrid control methods (20).

1.2. Literature review and previous work

A microgrid control system should ideally include: a) voltage and frequency control for various DERs, b) power balance between generation and load, c) economic dispatch for participation in power markets, and d) smooth transition between grid-connected and islanded modes for satisfactory system performance. The work presented in this paper focuses on employing a MPC scheme for secondary level control and re-synchronizations applied to a microgrid with a gas turbine-based synchronous generator, a PV unit, and a BESS unit, addressing features a), b), and d). Economic dispatch (feature c) is outside this study's scope.

The most widely referenced work on topics a) and b) is likely review paper (16). It delves into significant issues and challenges in islanded microgrid control, presenting cutting-edge control strategies. Review paper (21) comprehensively examines islanded microgrid secondary control architectures and strategies. The authors categorize secondary control strategies into three groups based on communication infrastructure: centralized, distributed, and decentralized. Despite ongoing research in distributed and decentralized methods, contemporary microgrids predominantly employ a centralized secondary control strategy, as highlighted in (22). This preference is attributed to the ease of design and operation offered by the use of Centralized Energy Management Systems (EMS) (23). Consequently, this paper embraces a centralized secondary-level controller for islanded microgrids. Paper (24) discusses a distributed control strategy for droop-controlled generation units in microgrids. Each inverter-based generation unit features three droop controllers for frequency, voltage, and reactive power sharing. Notably, this method's applicability is limited to microgrids with exclusively inverter-based DERs. In another example, employing MPC as an optimal control strategy for islanded microgrids, paper (25) outlines a secondary control approach for frequency restoration. The study compares two strategies: 1) MPC, and 2) Smith predictor-based controller. The robustness of the algorithm was tested including scenarios with communication delays, and the MPC-based controller exhibited the highest robustness. However, it should be noted that the control strategies discussed in all references are tailored to inverter-based resource generation units, ignoring the prevailing use of conventional power generation units in real-world microgrid deployments, i.e., gas and steam (26). Consequently, the applicability of such control strategies in microgrids becomes limited, especially in microgrids that are in regions with harsh winter conditions. Microgrids that are located in cold places usually have small-scale combined heat and power turbines that play a vital role in both power production and heating (27).

Concerning topic d), the traditional method for re-synchronizing synchronous generators involved manual or automatic synchronizers, discussed

in (28; 29). Initially applied in early microgrids with only synchronous generators, this approach is inadequate for modern microgrids with diverse DERs. Centralized EMS and active synchronization strategies (30; 31; 32) offer adaptable solutions for multiple DERs, especially in contemporary microgrids.

Finally, as noted in (33), while MPC is still in its early stages of implementation in microgrids, it shows promise as a control method for tasks like voltage and frequency regulation, power flow management, and economic optimization. However, given its emerging status in microgrid contexts, there remain numerous challenges to address, including refining models for better accuracy and quality, as well as ensuring stability in autonomously MPC-controlled microgrids. These are some of the challenges that the current paper addresses. As pointed out in (33), on the topic of secondary control strategies utilizing MPC in microgrids, existing research can be divided into two groups: 1) converter/equipment level MPC (34; 35; 36; 37), and 2) MPC at the grid level (38; 39; 40; 41; 42; 43). In the first group, converter-level MPC focuses on applying MPC within the controllers of power electronics-based devices, which limits its application to inverter-based DERs only. Among the grid-level MPC papers, which align with the overall goal of our work, the work in (41; 42; 43) are the closest to our research. Despite the high-level similarity in the goals and use of MPC, there are significant simplifications in all the studies conducted. The authors assumed a stable and steady-state initial condition for their islanded microgrid system at the beginning of their MPC optimizations, while also neglecting their re-synchronization to the utility grid. Addressing these assumptions sets our proposed control architecture apart.

In contrast, our proposed control architecture is versatile, catering to both optimal islanded operation and re-synchronization. The MPC approach implemented herein is capable of stabilizing the grid immediately after the islanding condition, optimizing power balance during the islanded condition, and priming the islanded microgrid for re-synchronization. On the modeling and computational side, while leveraging the object-oriented nature of the Modelica language, our models are generic and reusable, while at the same time aligning with industry-standard conventions used by the *de facto* software tools used by the power industry, like Siemens PTI PSSE (44). The similarity to PTI PSSE aims to minimize potential resistance to adopting Modelica-based simulation results by the power sector, as documented in (45).

1.3. Contributions

The main contributions of this article are:

1. An all-in-one MPC-based control architecture that provides an optimal microgrid secondary level control during islanded conditions, as well

as an optimal microgrid resynchronization with a mixed DER energy sources.

2. A comparison analysis between state-of-the-art methods for both secondary control and resynchronization against the proposed MPC algorithm.
3. For modeling and simulation purposes, this paper proposes an innovative and MPC-friendly simulation and optimization framework, utilizing phasor-domain models from the open-source OpenIPSL Library (46; 47), and MATLAB's Model Predictive Control Toolbox (48; 49).

1.4. Paper Structure

The remainder of this paper is organized as follows: Section 2 defines the basic concepts behind microgrid control from the perspective of secondary level control during an islanding event, islanded operation and resynchronization; Section 3 defines the microgrid and utility grid models and how they were constructed with the OpenIPSL Modelica Library; Section 4 lays out the MPC problem formulation for a microgrid with three DER sources, and also explains how the proposed "Dymola + MATLAB MPC" simulation and optimization framework operates; Section 5 describes simulation results from case studies that aim to validate the MPC-based control scheme for secondary level and re-synchronization control; and lastly Section 6 ends with conclusions.

2. Microgrid Control Basic Concepts

2.1. Microgrid Control

When a microgrid is disconnected from the main grid (islanded mode), the microgrid EMS has to maintain the isolated microgrid operational, adhering to system performance requirements. For medium level grids, which is the case of the microgrid in this work (ranging from 1 kV - 35 kV), the power quality requirements that the microgrid must abide are:

- **Voltage -** Rapid voltage changes in the grid, mainly caused by load variations in the network must be within a 5% margin of the nominal voltage level.

- **Frequency -** For systems with distributed energy resources, which is the case of microgrids, the frequency must be within a tight frequency band of $\pm$ 0.5 Hz from the nominal frequency of the system. This condition will be enforced during the pre-, during, and post-islanding of the microgrid.

The quality criteria defined above can be found in power system energy quality standards IEEE Std 1547.4-2011 (50) and Standard EN 50160 (51).

2.2. Microgrid Re-synchronization

When the microgrid undergoes re-synchronization, the EMS tracks the main grid side voltage phasor at the point of common coupling between the microgrid and the utility grid. A successful re-synchronization achieves minimal power oscillations in both systems, and it is conducted by measuring the voltage phasor at the utility bus side. A smooth connection is guaranteed when the voltages at both buses are similar in magnitude and phase (14). Furthermore, the frequency deviation between the two systems must be as small as possible (14; 19). Additionally, proper re-synchronization also reduces unnecessary torsional stress on the synchronous generator rotor. Elevated torsional stress in rotors can reduce the expected life time of the equipment, resulting in the loss of millions of dollars. Thus, the maximum acceptable variation in a generator's power injection at the re-synchronization instant (for the case of steam turbines) is 50% of its pre re-synchronization active power (52).

2.3. Microgrid Operation Modes

Figure 1 illustrates the various operating modes or stages that a microgrid may undergo, summarized as follows:

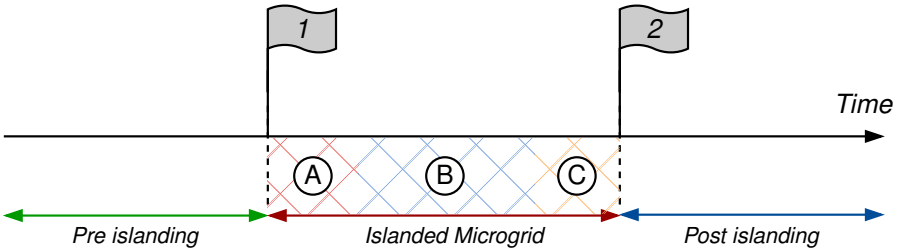

Figure 1: Microgrid operation modes.

Ⓐ When the microgrid is islanded from the grid (Flag 1), the control objective is to maintain the microgrid operational, exemplified by the cross-hatched area Ⓐ. The loss of connectivity to the utility grid can result in a deficit/surplus of power in the microgrid, which can lead to excessive deviations in frequency in both transient and steady-state. Thus, the control strategy in area Ⓐ is mainly concerned with keeping the microgrid online and resisting initial transients. As a result, area Ⓐ control requires rapid frequency and voltage support, guaranteed via short-term ancillary services utilizing the MPC controller structure.

Ⓑ If the initial objective of keeping the microgrid operational is achieved, the microgrid must keep energy within a delimited range in order to sustain energy quality and reliability (50; 51), exemplified by the cross-hatched area Ⓑ. This stage of the control is responsible for balancing

the power dispatch in the microgrid, guaranteed by the secondary control level. Area Ⓑ control is mainly dictated by long-term ancillary services, specifically load following.

Ⓒ Once the utility grid signals that it is ready to re-connect the microgrid, the microgrid transitions to the last stage, which is microgrid re-synchronization, exemplified by the cross hatched area Ⓒ. Once the microgrid has met the system performance requirements for synchronization (14), a command must be issued for the main utility circuit breaker to close (Flag 2), ending the islanded operation of the microgrid.

With the MPC control strategy proposed in this work, the microgrid is capable of achieving stages Ⓐ, Ⓑ, and Ⓒ with only one controller architecture, rather than three distinct control stages as proposed in the literature (19; 12; 18).

3. Microgrid Structure and Modeling

3.1. System Model Blueprint

Figure 2 illustrates the configuration of the microgrid system and its connection to the main grid. The microgrid includes a 10 MW combustion-based synchronous generator with primary-level control, a PV plant, and BESS units with active/reactive power controls. The renewable sources are rated at 5 MW. The utility grid model consists of a power distribution system, a hydro power plant, and associated infrastructure. In this setup, the synchronous generator dictates the voltage and frequency within the microgrid, while the renewable DERs operate as "grid-following" components. This system model aims to examine microgrid interaction with nearby energy sources and simulate both joint operation during re-synchronization and isolated operation when the microgrid operates independently due to circuit breaker tripping.

MPC optimization algorithms generate updated system input values that steer the system towards a user-defined goal. Thus, for secondary control and re-synchronization purposes, the idea is to use MPC to update the set point values for specific variables within each of the DER's primary control loops. For the microgrid model studied in this work, there are five input variables (which dictate the reference values in each DER source), characterized by the variables u_1 through u_5. These set point values are herein referred to as the "manipulated variables" that the MPC algorithm will provide to steer the microgrid toward a desired target. Rather than updating the reference value itself, the manipulated variables u_1 through u_5 are added

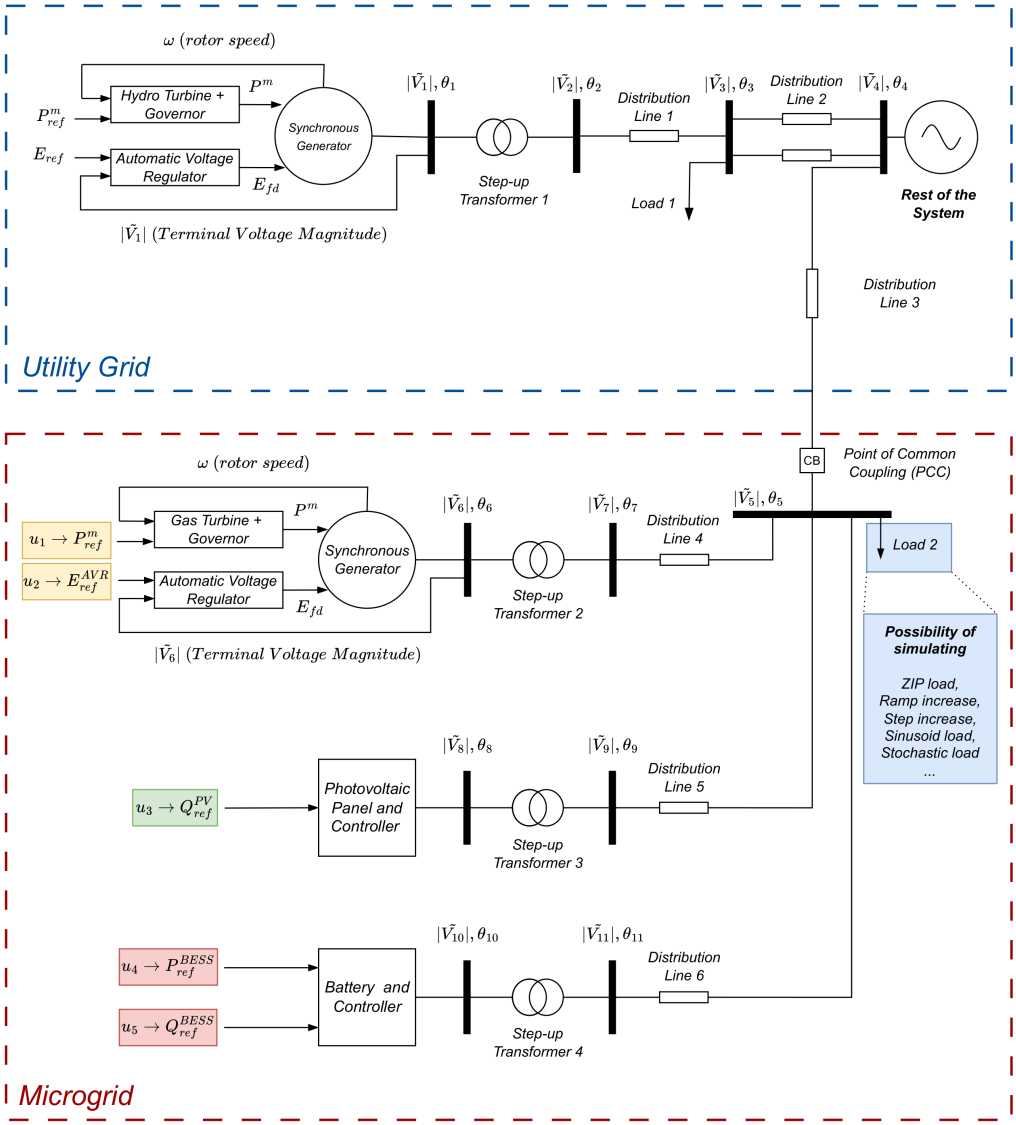

Figure 2: Microgrid system schematic diagram.

to the pre-islanded reference value, which originates from a power flow solution. This was implemented to facilitate the simulation procedure. For the synchronous generation unit, the manipulated variables are mechanical power reference and excitation system voltage reference. Since PV systems are non-dispatchable units, typically set to maximum active power injection using a maximum power point tracking algorithm, this leaves reactive power control as the only manipulated variable. BESS, on the other hand, is dispatchable; therefore, the manipulated variables are active and reactive power references. The microgrid is interconnected to the utility grid through a single feeder transmission line, represented by Distribution Line 3 and its point

of common coupling (PCC), which is equipped with a circuit breaker. Both the microgrid and the utility grid have a load that represents an aggregate of electrical loads. Load 1 is the aggregated load of a passive distribution network, and Load 2 is the aggregated load within the microgrid. In order to test the effectiveness of the MPC controller, the authors added stochastic features to Load 2 as well as irradiance for the PV unit. More information is presented in the following sections.

3.2. Modeling using Modelica and OpenIPSL

The system in Fig. 2 was modeled using the OpenIPSL Modelica Library, as shown in Fig. 3. Modelica, an open-source language, facilitates detailed modeling of physical systems, including electrical, mechanical, and control systems (53; 54). OpenIPSL is a library of power system component models written in the Modelica language that can be used for power system dynamic analysis, such as phasor time-domain simulations (47; 46).

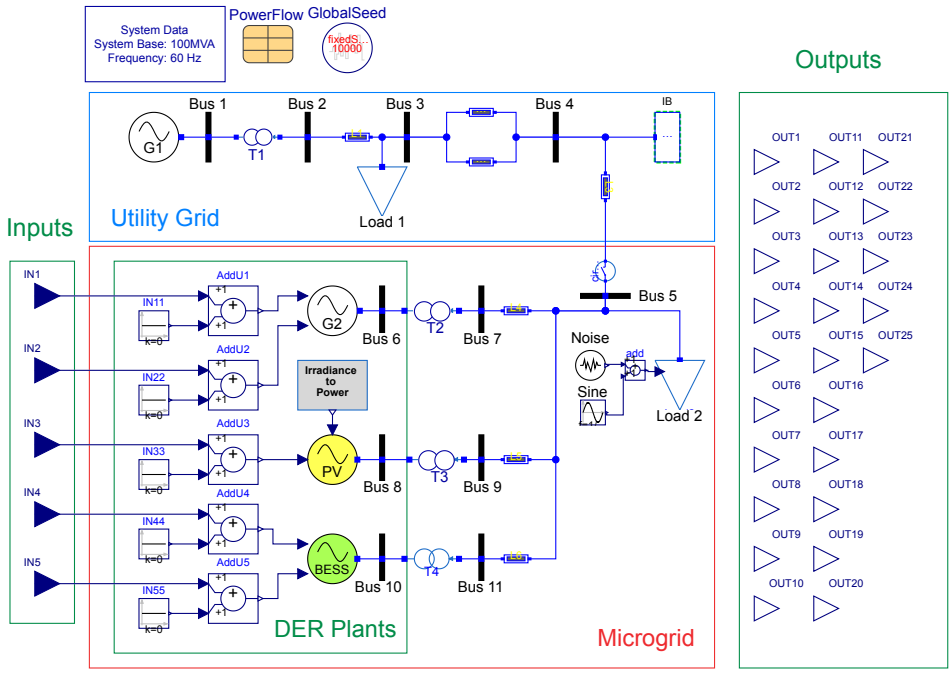

Figure 3: Microgrid system in Dymola utilizing OpenIPSL.

The models developed in OpenIPSL are meant for transient stability analysis. Thus, the time scale of interest ranges from 0.01 s to 10 s or, which is equivalent to analyzing transients from 0.1 Hz to 100 Hz (55). Therefore, fast dynamics related to switching components, and electromagnetic events are not taken into consideration. The microgrid is represented by

the components outlined by the continuous red line, while the utility grid is represented by components outlined by the continuous blue line. The microgrid generator model, **G2**[1] in Fig. 3, uses the **GENROU**, **SEXS**, and the **GAST** models (44). The **PV** system is modeled by the combination of components **REGCA**, **REECB**, and **REPCA** described in (56). An add-on was implemented to emulate irradiance to power conversion based on HOMER Energy software (57) guidelines (Appendix E), and is connected to the PV model. The **BESS** unit is modeled by the same components as the **PV** source, with the difference being the usage of **REECC** component and the lack of the irradiance to power block. The Western Electricity Coordinating Council (WECC) created these renewable components as generic models to emulate most inverter-based resources in the field (58; 59; 56). The utility grid generator **G1**, modeled as a hydro-turbine generation units, is modeled by the **GENSAL**, **SEXS**, and the **HYGOV** component models. Network components are modeled by algebraic equations, which is an adequate simplification, given the quasi-steady value of frequency in the system. All components utilized in Fig. 3 are standard power system dynamic models that are ubiquitously used and trusted by the power community.

3.2.1. Microgrid Generation Unit Equations and Block Diagrams

Modelica offers flexibility in modeling, allowing the creation of models using mathematical equations, transfer function blocks, and more. For **G2**, the **GENROU** model was implemented with differential-algebraic equations, while the **GAST** and **SEXS** components used transfer functions. The block diagrams for **G2**'s gas turbine speed governor and AVR systems are presented in Appendix C and Appendix D. The total number of states for the **G2** model is 11 (6 in **GENROU**, 2 in **SEXS**, and 3 in **GAST**).

For the renewable models, dynamics were built exclusively with transfer function blocks. These models were designed to be generic, allowing users to choose the control logic for the renewable source. Depending on the control selection, logical switches within the model toggle "on" or "off," altering the general block diagram accordingly. There are 8 different reactive power control options; this study selected Voltage/Reactive Power control mode for both the **PV** and **BESS** modules, as it is the most common configuration for inverter-based resources. The block diagrams for the renewable models are shown in Appendix E and Appendix F. The total number of states in the **PV** model is 12, while the **BESS** model has 13.

This paper focuses on the application of the MPC algorithm for both microgrid islanding and re-synchronization, assuming that the Proportional and Integral (PI) controllers in the PV and BESS models are properly tuned

[1]The **bold** font is used to denote Modelica component names in the system in Fig. 3.

to avoid detrimental interactive loops. The user must decide which of the two controls operates at a higher speed while the other is slower. The fast-acting PI controller, the secondary controller, is tuned first, followed by the slower PI controller, the primary controller. For both renewable sources, the reactive power PI controller is the fast-acting loop, while the voltage PI controller is slower. For more detailed information on cascading controllers, refer to *Principles and Practices of Automatic Process Control* (60). For further information on the equations and models comprising generator G2 and the renewable energy sources, refer to (44).

3.2.2. MPC Prediction Model

Because the optimization algorithm in this paper is based on a linear MPC, it becomes imperative to linearize the entire set of differential equations that make up the microgrid model, specifically the energy sources. This involves deriving the linear dynamic matrix (or state matrix) denoted as $\mathbb{A}$, the controller matrix (or input matrix) denoted as $\mathbb{B}$, and the state measurement matrix (or output matrix) denoted as $\mathbb{C}$ for the model. Whether the equations are presented in the time or frequency domain, Dymola facilitates this linearization process at any specific time by utilizing the functionalities provided by the Modelica_LinearSystems2 Library (61).

It is important to acknowledge that while estimating the unobserved states of the gas-turbine-based synchronous generator unit **G2** is achievable through a set of carefully chosen measurements, estimating all dynamic states from the **PV** and **BESS** models using commonly measured variables such as bus voltage and current/power injections is not possible. Estimating the states of the PI controllers for both renewable sources (Appendix E and Appendix F) is not achievable. To overcome this issue, a reduced-order model was implemented for both renewable energy sources. In this new model, the internal states can be estimated by actively measuring active/reactive power and terminal currents during the simulation of the full-order model. Subsequently, the reduced order model is utilized to formulate the MPC prediction model, which is then applied in the optimization step. The reduced-order model for both renewable sources is detailed in Appendix G.

To streamline this process, Modelica scripts (54) were employed to automate linearization tasks. These scripts facilitated the storage of initial and final model parameter values, modification of differential equation initial conditions, execution of functions available in Dymola's Advanced Programming Interface (API) (62), and data exchange with MATLAB.

4. MPC-based Controller Architecture for Microgrid Resilience

As discussed earlier, MPC-based control schemes are increasing in popularity and are even considered potential successors to PID controllers in

complex industrial applications (63). MPC algorithms, different from their PID counterparts, are algorithms that generate optimal open-loop trajectory calculations where stability is guaranteed via the terminal cost condition. The major advantage of MPC is its inherent capability to optimize a particular system while also dealing with input/output constraints (64). Because of its open-loop optimization nature, MPC controllers fit the online optimization group of algorithms, meaning that they optimize the system in a recurring fashion and, with adequate engineering, can even be used in real-time. The following sections will describe key aspects of the MPC controller in the sense of microgrid resiliency.

4.1. MPC Constraints

The power generation units in the microgrid must operate within its maximum and minimum power output values. In doing so, power quality must always be ensured, maintaining three key variables, voltage magnitude, voltage phase angle, and system frequency, within acceptable ranges (65). According to the standards described in Section 2, the rated frequency of the supply voltage is 50/60 Hz with a frequency deviation limited to ± 0.5 Hz, and the voltage magnitude should always be within 95% to 105% of its nominal voltage magnitude. The power output of the synchronous generator is related to the mechanical power delivered by the turbine rotor shaft, and it is also bounded by the equipment's own physical limits. The same is true for the renewable energy sources, active and reactive power output is tied to the rated power of each component. In order to avoid computational issues that can arise when solving the online Quadratic Programming (QP) problems that are part of the MPC algorithm, the rate of change for G2's manipulated variables and the output variables must be defined as a soft constraint. This means that Eqs. (2),(4), (9), and (10) are set as soft constraints. To avoid aggressive increments in the manipulated variables the cost function weights must be carefully set (more information in Section 4.2). Because inverter-based resources are power electronics-based equipment with response times within milliseconds, it can be assumed that there is no limit to their manipulated variable's rates. Thus, the set of MPC constraints for secondary control and re-synchronization are defined as follows:

$$P^m_{min} \leq P^m_{ref} \leq P^m_{max} \tag{1}$$

$$\Delta P^m_{min} \leq \Delta P^m_{ref} \leq \Delta P^m_{max} \tag{2}$$

$$E^{AVR}_{min} \leq E^{AVR}_{ref} \leq E^{AVR}_{max} \tag{3}$$

$$\Delta E^{AVR}_{min} \leq \Delta E^{AVR}_{ref} \leq \Delta E^{AVR}_{max} \tag{4}$$

$$Q^{PV}_{min} \leq Q^{PV}_{ref} \leq Q^{PV}_{max} \tag{5}$$

$$P_{min}^{BESS} \leq P_{ref}^{BESS} \leq P_{max}^{BESS} \tag{6}$$

$$Q_{min}^{BESS} \leq Q_{ref}^{BESS} \leq Q_{max}^{BESS} \tag{7}$$

$$\sqrt{P_{gen}^2 + Q_{gen}^2} \leq S_{rated} \quad \text{for G2, BESS, and PV} \tag{8}$$

$$f_{min} \leq f \leq f_{max} \tag{9}$$

$$V_{min}^{Bus5} \leq V^{Bus5} \leq V_{max}^{Bus5} \tag{10}$$

in which Eqs. (1) and (2) represent G2's power limit and rate of change limit respectively, while Eqs. (3) and (4) represent the maximum operating limit of the field voltage allowed by G2's and the rate of change, respectively. Meanwhile, Eq. (5) is the PV reactive power limit, and Eqs. (6) and (7) represent the active/reactive power limits of the BESS. For each of the generation units, Eq. (8) represents the apparent power limits based on their nominal rated power. Finally, to keep the system frequency within permissible operation limits, Eq. (9) is used, and lastly, Eq. (10) defines permissible range of the magnitude of the voltage for the PCC bus as measured from the microgrid side.

4.2. MPC Cost Function and Algorithm Stability

During each control interval, the MPC algorithm solves a quadratic program (QP), which is an optimization problem. The resolution identifies the manipulated variables (control inputs) to apply in the plant until the subsequent control interval. (64). The cost function adopted in the MPC optimization step of this work is defined as:

$$J(u^*) = J_y(u^*) + J_u(u^*) + J_{\Delta u}(u^*) + J_\varepsilon(u^*) \tag{11}$$

where $J_y(u^*)$ is the output reference tracking cost, $J_u(u^*)$ is the input variable tracking cost, $J_{\Delta u}(u^*)$ is the input move suppression cost, and $J_\varepsilon(u^*)$ is the constraint violation cost term (49). The $J_u(u^*)$ cost term penalizes the overall cost function $J(u^*)$ if there is an input reference value attributed to the controller. For the simulation examples in this paper, this cost function does not affect the overall cost function because there are no input references in the defined problem. The variable $u^* \in \mathbb{R}^{n_i \times n_c}$ is the QP decision matrix, representing the entirety of the manipulated variables for the prediction length $\{k, \cdots, k+p-1\}$, as shown in equation (12),

$$u^* = \begin{bmatrix} u(k \mid k) & u(k+1 \mid k) & \cdots & u(k+p-1 \mid k) \end{bmatrix} \tag{12}$$

where k represents the discrete instant in time, n_i represents the number of controllable inputs, n_c is the size of the control horizon (a parameter chosen by the user), and p represents the size of the prediction horizon.

The stability of the MPC algorithm itself is ensured by the terminal constraint theorem, which guarantees stability regardless of the horizon length, as long as a terminal constraint is introduced to enforce the state reaching a specified value at the final moment of the prediction horizon (64). Each term in the cost function is quadratic, turning the optimization process into a quadratic programming algorithm (66). For the purpose of this work, the cost function places particular emphasis on two terms in the MPC-based secondary control and re-synchronization scheme, i.e., the output reference tracking cost, denoted as $J_y(u^*)$, and the manipulated variable move suppression cost, denoted as $J_{\Delta u}(u^*)$, presented in Eqs. (13) and (14).

$$J_y(u^*) = \sum_{i=1}^{p} \left\{ \left(w_i^{V_5} \Delta V_i^{(5)} \right) + \left(w_i^{\theta_5} \Delta \theta_i^{(5)} \right) + \left(w_i^{f} \Delta f_i \right) \right\}^2 \tag{13}$$

$$\begin{aligned} J_{\Delta u}(u^*) = \sum_{i=1}^{p} \Bigg\{ & \left(w_i^{\Delta P_{ref}^m} \Delta P_{ref_i}^m \right) + \left(w_i^{\Delta V_{ref}} \Delta V_{ref_i} \right) + \left(w_i^{\Delta Q_{ref}^{PV}} \Delta Q_{ref_i}^{PV} \right) \\ & + \left(w_i^{\Delta P_{ref}^{BESS}} \Delta P_{ref_i}^{BESS} \right) + \left(w_i^{\Delta Q_{ref}^{BESS}} \Delta Q_{ref_i}^{BESS} \right) \Bigg\}^2 \end{aligned} \tag{14}$$

In Eq. (13), $\Delta V_i^{(5)}$, $\Delta \theta_i^{(5)}$, and Δf_i are the differences between the three observed variables and the reference values used as the MPC target, defined as:

$$\begin{aligned} \Delta V_i^{(5)} &= \left[V_5^{ref}(k+i \mid k) \; - V_5^{out}(k+i \mid k) \right] \\ \Delta \theta_i^{(5)} &= \left[\theta_5^{ref} \; (k+i \mid k) \; - \; \theta_5^{out}(k+i \mid k) \right] \\ \Delta f_i &= \left[f^{ref} \; (k+i \mid k) \; - \; f^{out}(k+i \mid k) \right] \end{aligned} \tag{15}$$

The weights $w_i^{V_5}$, $w_i^{\theta_5}$, and w_i^{f} from Eq. (13) indicate how strongly the MPC control algorithm prioritizes reaching the reference values, penalizing greatly the cost function when ΔV, $\Delta \theta$, and Δf are not null.

In Eq. (14), $\Delta P_{ref_i}^m$, ΔV_{ref_i}, $\Delta Q_{ref_i}^{PV}$, $\Delta P_{ref_i}^{BESS}$, and $\Delta P_{ref_i}^m$ are the differences between subsequent values of the manipulated variables, calculated through the optimization stage. These variables are defined as:

$$
\begin{aligned}
\Delta P^{m}_{ref_i} &= \left[P^{m}_{ref}(k+i \mid k) \; - P^{m}_{ref}(k+i-1 \mid k)\right] \\
\Delta V_{ref_i} &= \left[V_{ref}(k+i \mid k) \; - \; V_{ref}(k+i-1 \mid k)\right] \\
\Delta Q^{PV}_{ref_i} &= \left[Q^{PV}_{ref}(k+i \mid k) \; - \; Q^{PV}_{ref}(k+i-1 \mid k)\right] \\
\Delta P^{BESS}_{ref_i} &= \left[P^{BESS}_{ref}(k+i \mid k) \; - \; P^{BESS}_{ref}(k+i-1 \mid k)\right] \\
\Delta Q^{BESS}_{ref_i} &= \left[Q^{BESS}_{ref}(k+i \mid k) \; - \; Q^{BESS}_{ref}(k+i-1 \mid k)\right]
\end{aligned}
\tag{16}
$$

The weights $w_i^{\Delta P^m_{ref}}$, $w_i^{\Delta V_{ref}}$, $w_i^{\Delta Q^{PV}_{ref}}$, $w_i^{\Delta P^{BESS}_{ref}}$, and $w_i^{\Delta Q^{BESS}_{ref}}$ from Eq. (14) indicate how aggressive the increment between successive input values throughout the prediction length should be. Many applications prioritize minimal adjustments (moves) in manipulated variables. This is especially true when dealing with uncertainty in the model, stochastic loads, and measurement noise. The sum in Eqs. (11) spans the entire simulation period, where the optimization problem is then formulated and solved in MATLAB. The resulting QP problem is posed with the objective of minimizing the overall cost function. For more details on the optimization step, refer to (48; 49).

4.3. Optimization Problem

The optimization problem for microgrid resiliency is thus formulated as follows:

$$
\begin{aligned}
\min_{u^*} \quad & J\left(u^*\right), \\
\text{s.t.} \quad & P^{m}_{min} \le P^{m}_{ref} \le P^{m}_{max}, \\
& \Delta P^{m}_{min} \le \Delta P^{m}_{ref} \le \Delta P^{m}_{max}, \\
& E^{AVR}_{min} \le E^{AVR}_{ref} \le E^{AVR}_{max}, \\
& \Delta E^{AVR}_{min} \le \Delta E^{AVR}_{ref} \le \Delta E^{AVR}_{max}, \\
& Q^{PV}_{min} \le Q^{PV}_{ref} \le Q^{PV}_{max}, \\
& P^{BESS}_{min} \le P^{BESS}_{ref} \le P^{BESS}_{max}, \\
& Q^{BESS}_{min} \le Q^{BESS}_{ref} \le Q^{BESS}_{max}, \\
& \sqrt{P^2_{gen} + Q^2_{gen}} \le S_{rated} \quad \text{for G2, BESS, and PV,} \\
& f_{min} \le f \le f_{max}, \\
& V^{Bus5}_{min} \le V^{Bus5} \le V^{Bus5}_{max}.
\end{aligned}
\tag{17}
$$

where Eq. 17 is then solved at each time step of the MPC-based control scheme by QP. The optimizer used is the the built-in active-set QP solver supported by MATLAB[2] described in detail in (67).

[2]See the built-in active-set QP solver supported by MATLAB's documentation online at: `https://www.mathworks.com/help/mpc/ug/qp-solver.html`

4.4. The proposed simulation and optimization framework

Figure 4 displays a pictorial representation of the two layers that comprise the proposed simulation and optimization framework used to study the MPC control scheme for secondary control and re-synchronization.

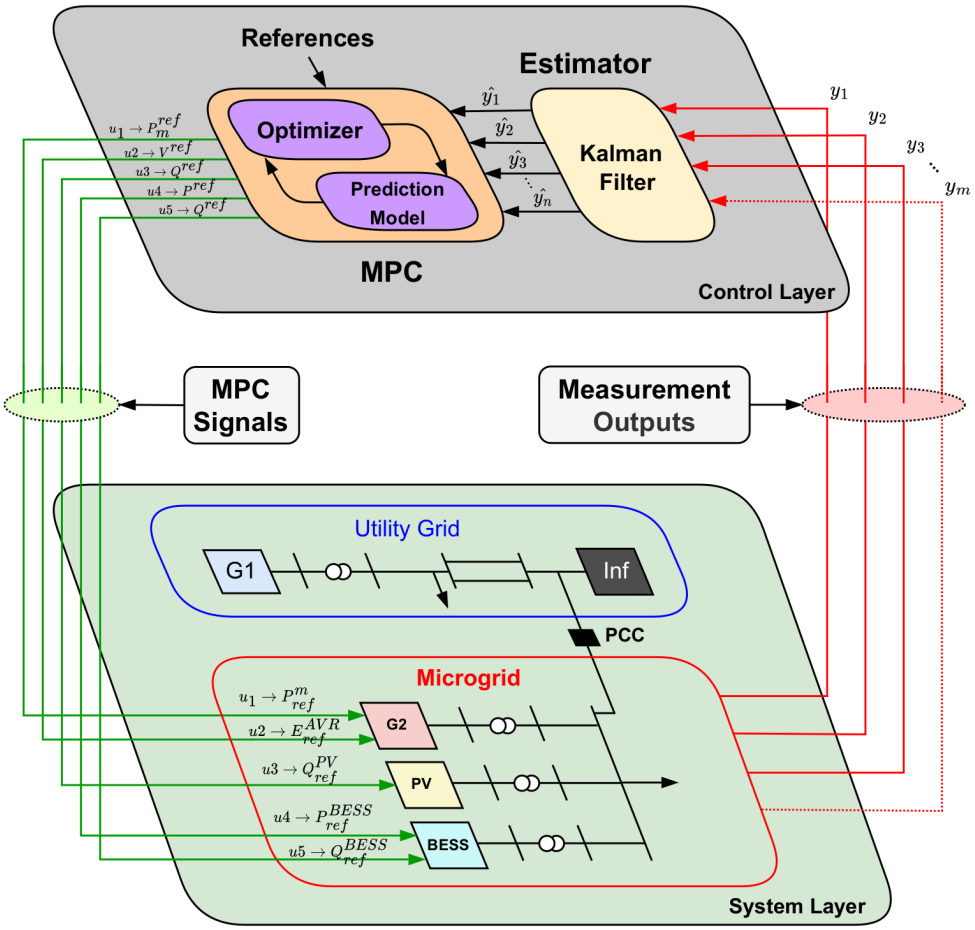

Figure 4: System layer and MPC control layer representation.

4.4.1. System Layer

For the purposes of this work, the system layer is defined by the electrical system model, comprised of a utility grid and a neighboring microgrid. The model was developed utilizing components from the OpenIPSL Library as described in Section 3.2. To provide the MPC algorithm with meaningful model information, Dymola is used in combination with a Modelica script that performs the following tasks:

1. Run the dynamic simulations of the entire simulation scenario.
2. Iteratively initialize the system model for every simulation window based on the final value of the states from the previous simulation.

3. Automate the process of linearizing the DER sources in the Microgrid.
4. Track the "measurement" output values of the microgrid for state estimation.
5. Keep track of the derivatives of the states used to update the initialization.

This information is exchanged with MATLAB which is used to implement the *Control Layer* of Fig. 4.

4.4.2. Control Layer

The control layer was developed using MATLAB and its Predictive Control Toolbox (49). The state estimation process utilizes the linearized model of the microgrid containing the reduced-order renewable models (see Appendix G for details). The estimator estimates the states of all generation units, based on measured outputs and the current input signal, and determines the derivative of the estimated and filtered states. The estimator of this work is a Kalman Filter, with the estimation step implemented utilizing MATLAB and its *lqe* function (68). A new initial condition is set as the nominal starting value for the MPC algorithm, which utilizes the microgrid model with reduced order renewables as the prediction model for the optimization step. The prediction model is in the state-space form which is automatically derived from the Modelica model (see (61)), and the optimizer produces a solution to the QP problem with the *sim* function from MATLAB (68). The list of measurement outputs from the microgrid that are used in the state estimation process is summarized below:

- **G2**: rotor speed, excitation system output voltage, gas turbine exhaust temperature, generator electrical power, rotor shaft mechanical power, terminal voltage phasor (magnitude and angle), and terminal current phasor (magnitude and angle).
- **PV**: electrical power, terminal voltage phasor (magnitude and angle), and terminal current phasor (magnitude and angle).
- **BESS**: electrical power, terminal voltage phasor (magnitude and angle), and terminal current phasor (magnitude and angle).
- **Bus 5**: voltage magnitude and angle.

From the above measurement data, the discrete-time state-space system matrices $\mathbb{A}, \mathbb{B}, \mathbb{C}$ for the microgrid are obtained, which guarantees that the system is controllable and observable, leading to the adequate estimation of the microgrid states through the Kalman Filter (69). The Kalman Filter-base state estimation (SE) is applied at a tick rate faster (e.g. of 0.05 sec.) than the rate for the MPC's manipulated variable update (e.g. of 0.5 sec.). The

reason for the use of different update rates for the SE and the MPC is that at each optimization step during the simulation, it is necessary to update both the nominal initial condition for the state and the state derivatives.

For completeness, Appendix A displays a flow chart that describes the step-by-step strategy adopted in the new MPC-based secondary control, while Appendix A is an overview of the overall implementation procedure for the MPC-based microgrid optimization environment simulator. Although the framework proposed herein is entirely used for simulation and optimization and is primarily meant to study the proposed MPC-based control scheme, one could see this as the basis for developing a similar solution within a microgrid's EMS system, however, such engineering enterprise is out of the scope of this work.

5. Simulation Results

In order to demonstrate the capability of the developed MPC secondary and re-synchronization controller, the authors devised a set of simulations that are presented in this section and are named "Tests". Tests 1 - 3 were conducted on the microgrid system presented in this work, where the system parameters are presented in Appendix H, Appendix I, and Appendix J. Tests 4 - 6 were conducted on a real university campus microgrid model. For greater detail on the university campus model, refer to paper (70). The authors utilized the *mpcDesigner* function in MATLAB to design, simulate, and test various configurations of the MPC controller. Through this iterative process, the authors refined the configurations until achieving optimal values. The final configuration was selected to balance closed-loop performance and robustness against potential measurement uncertainties. For more information, refer to (71). The calculation for the average time of the Kalman Filter computation, and MPC optimization calculation for all the tests in this section were run utilizing a computer with the following specifications: Windows 10, Intel®i7 2.60GHz, 32 GB Ram.

5.1. Test 1 - Islanding Scenario with Synchronous Generator and Recursive Feasibility Check

This section is organized into three parts. First, the motivation and scope of the test are described. The operating conditions and constraints are then specified, followed by the results and analysis for the islanding scenario.

5.1.1. Motivation and Scope

Test 1 highlights the MPC controller's effectiveness in sustaining microgrid operation during islanding (operation mode Ⓐ in Fig. 1). This test examines a scenario in which only the conventional synchronous generator

is in operation. In addition, this test will serve as a reference when contrasting the microgrid's performance in other subsequent tests where the PV and BESS are included, which will help to explore the potential benefits of exploiting these additional resources within the MPC.

Next, two simulations with similar pre-islanding states are explored: one without load shedding and the other with 50% of load shedding. This serves to determine the impact of load shedding on microgrid operation. Therefore, Test 1 validates the MPC framework during the mode (A) for the microgrid operating only with the conventional synchronous generator and experiencing load disturbance (load shedding) and load stochasticity. Finally, in both simulations, the recurrent feasibility check of the MPC optimization solution is performed. The recurrent feasibility check ensures the solution's feasibility by monitoring the output variables V_{Bus5}, θ_5, and f. If these values fall outside the acceptable range, the islanded microgrid fails to meet the quality constraints defined in Section 2.1. In such cases, external interventions are needed to restore feasibility, exemplified in Test 1 through load shedding.

5.1.2. Operating Conditions and Constraints

Table 1 displays the power dispatch pre-islanding scenario, while Table 2 displays the manipulated variable constraints.

Table 1: Dispatch scenario for Test 1.

Pre-islanding steady-state scenario [MW/MVar]							
G1	*G2*	*PV*	*BESS*	*Inf*	*Load 1*	*Load 2*	P_{45} *&* Q_{45}
54.06	5.00	0.00	0.00	0	50.00	9.00	4.00
7.49	1.76	0.00	0.00	15.79	10.00	2.95	1.27

Note: P_{45} and Q_{45} denote the active and reactive power flowing through the power line connecting **Bus 4**, and **Bus 5**, respectively (see Fig. 3). A positive value indicates that the microgrid imports power, while a negative value indicates that the microgrid exports power.

Table 2: Test 1 constraints.

MPC Manipulated Variable Constraints		
DER	*Hard Constraints*	*Soft Constraints*
G2	$2 \leq P^m_{ref} \leq 10$ [MW]	$-167 \leq \Delta P^m_{ref} \leq 167$ [kW]
	$0 \leq E^{AVR}_{ref} \leq 5$ [p.u.]	$-0.25 \leq \Delta E^m_{ref} \leq 0.25$ [p.u.]

In this test, G2 initially supplies 5 MW and 1.76 MVar, while the utility grid supplies the remaining power to match the demand of Load 2. Load 2 is modeled by a ZIP load with added noise to mimic load stochasticity. The standard deviation of Load 2 demand is $\delta = 0.0002$ with a sample period of 0.02 s. No measurement noise was included in the experiment. G2 has hard and soft constraints that are detailed in Table 2. For the prediction horizon

and control horizon selected for the optimization stage, a value of $n_p = 20$ and $n_c = 4$ were chosen respectively.

The target value for the output measurements during islanding is $V_{Bus5} =$ 1 p.u., $\theta_5 = 0°$, and $f = 60$ Hz. In reality, the MPC controller is capable of steering the system towards any value of θ_5 within the range of $[-180°, 180°]$. The choice for $\theta_5 = 0°$ in Test 1 is because it is an angle value near the pre-islanding initial condition. The microgrid is abruptly islanded at $t = 0.55$ s, which means that there was no time to plan ahead the pre-island power balance of the microgrid.

The MPC algorithm initiates the control sequence, updating the manipulated variables every 0.5 s, with a state estimation sub-tick of 0.05 s. It is worth mentioning that a controller input reference change of 0.5 s is motivated by real-world capabilities of field equipment, with Woodward Genset controllers such as the easYgen-3000XT Series being able to receive set-points externally using the Modbus communication in a range from 0.1 to 999 seconds (72). For this example, the average calculation times for the Kalman Filter and MPC Optimization stages were 0.0061 s, and 0.0073 s respectively, with a standard deviation of $\sigma = 0.0013$ s, and $\sigma = 0.008$ s respectively. This indicates that real-time application of the proposed secondary-level MPC controller in a microgrid setup is indeed feasible.

5.1.3. Results

Figures 5 and 6 show the feasibility check for both simulations (with and without load shedding) viewed through the three output variables V_{Bus5}, θ_5, and f. Meanwhile, Fig. 7 shows the manipulated variables (P^m_{ref}, and E^{AVR}_{ref}) and Fig. 8 the output variables (f, V_{Bus5}, and θ_5).

The feasibility of the microgrid's operating condition is tested recursively at the same tick rate as that of the state estimator, i.e. 0.05 sec. As observed in Figs. 5 and 6, for the case where no load shedding is applied (blue line), the output variables are moved outside the feasibility region. Due to the inherent rate of change of the active power reference P^m_{ref}, and the AVR voltage reference E^m_{ref}, the system is capable of reaching the target value; however, it spends a significant time outside of the feasible region, violating the power quality constraints defined in Section 2. To ensure that the constraints are respected, a load-shedding remedial action is performed to bring the system back to the feasible region as quickly as possible (red line). The 50% load shedding remedial action was chosen to emulate a reduction in electrical load to the bare minimum. This setup can be interpreted as keeping the most crucial electrical loads online amidst the post-islanding instance. The blue saw shape curve in Fig. 6, corresponding to the no load shedding scenario, reflects the angle lag of Bus 5 compared to the reference **IB**.

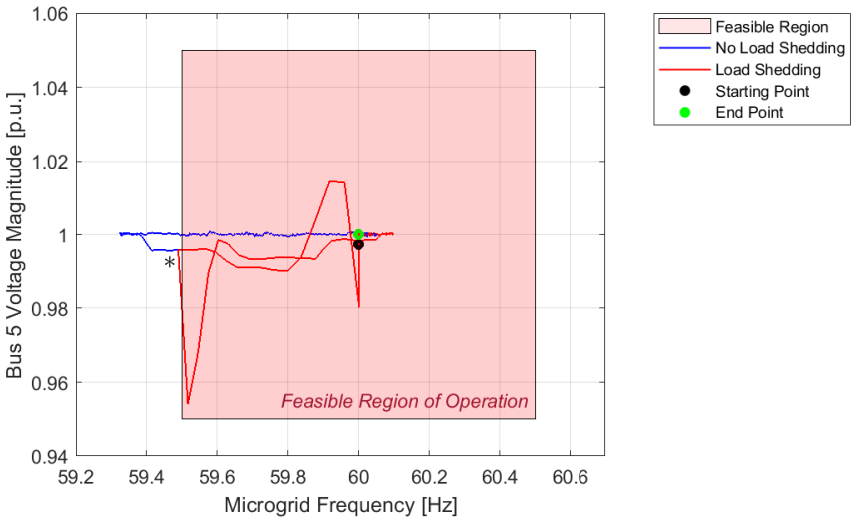

Figure 5: Bus 5 voltage magnitude and frequency feasibility region in Test 1.

In Figs. 5 and 6, there is a a bifurcation in the path of the output variables, depicted by the symbol "$*$". From the starting to the bifurcation point, the path that the output variables take in both scenarios is the same. Load shedding is applied to reduce the time spent outside the feasible region, resulting in different paths post bifurcation. It is also possible to track the bifurcation of output variables throughout time in Fig. 8 (a), and (c). The "$*$" symbol points to the exact moment in time that f breaches the feasible region of operation.

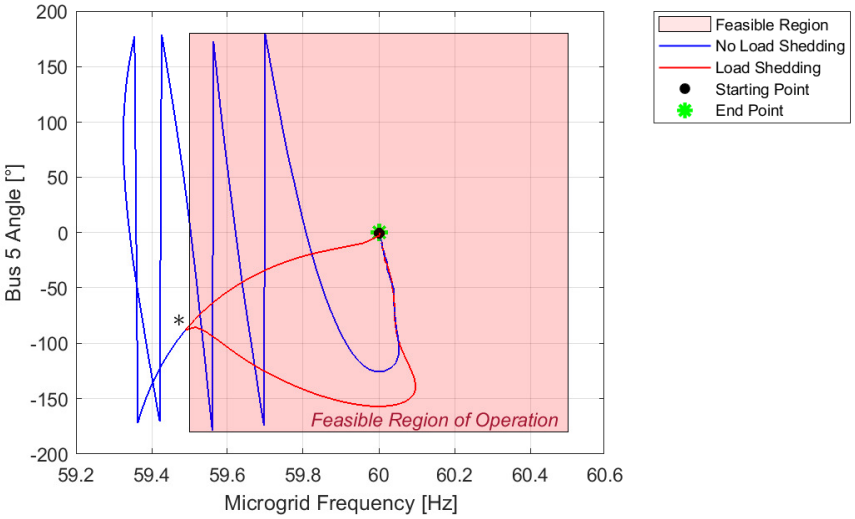

Figure 6: Bus 5 voltage angle and frequency feasibility region in Test 1.

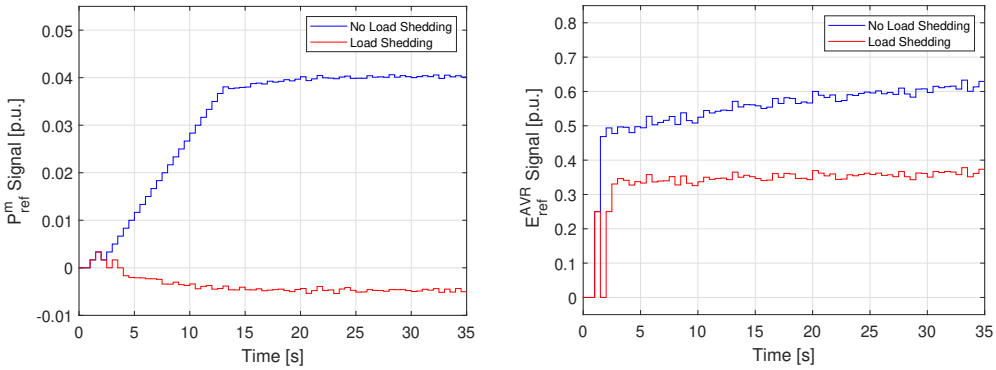

(a) P^m_{ref} input signal

(b) E^{AVR}_{ref} input signal

Figure 7: MPC manipulated variables P_m^{ref}, and E_m^{ref} in Test 1.

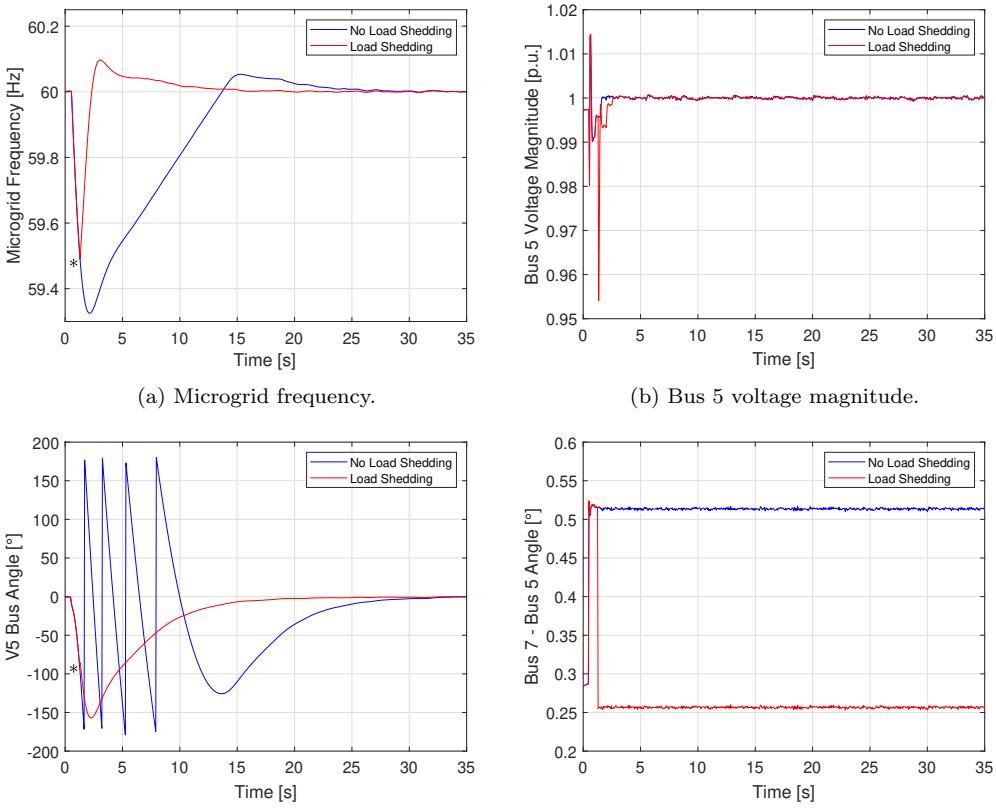

(a) Microgrid frequency.

(b) Bus 5 voltage magnitude.

(c) Bus 5 voltage angle.

(d) Angle difference between Bus 7 and 5.

Figure 8: MPC output variable, and angle difference ($\theta_7 - \theta_5$) in Test 1. The $*$ symbol points to the exact moment in time that f breaches the feasible region of operation.

Next, we analyze the results in Figs. 7 and 8. In Fig. 8 (c), the voltage angle in Bus 5 is presented for the no load shedding (blue line) and load

shedding (red line) cases[3]. The angle for the no-load shedding simulation displays a saw tooth response within the $[-180°, 180°]$ range, pointing to the fact that there the angle lags for roughly 8 seconds until ≈13 sec., when the P^m_{ref} starts reaching a steady-state (see the blue line in Fig. 7 (a)). Recall that the frequency is defined as $f = \frac{\partial\theta}{\partial t} + f_0$ where f_0=60 Hz and $\theta = \theta_5 = \angle\tilde{V}_5$. Thus, such angle variations are, in fact, a product of frequency control. Observe that frequency control is achieved by changing P^m_{ref} as shown in the blue line in Fig. 7 (a), resulting in the frequency reaching acceptable limits at ≈13 seconds as can be observed in Fig. 8 (c).

Load shedding, performed at $t = 0.55\ s$, speeds up the microgrid stabilization process, quickly reaching the reference frequency and angle references (see Figs. 8 (a) and 8(c)). In Fig. 8 (d) the voltage angle difference between **Bus 7** and **Bus 5** is constant during the steady-state operation of the microgrid, because both angles are referred to the **IB** reference angle during the islanding condition. The voltage reference E^{AVR}_{ref}, shown in Fig. 7 (b), is changed to control the magnitude of the measured voltage in **Bus 5**, which is seen to return to 1 p.u after the MPC adjusts the input reference value, as shown in Fig. 7 (b). Note that the impact of load shedding on the voltage is a substantial transient at $\approx 0.55\ s$, as shown in Fig. 8 (b). However, the MPC is able to provide adequate updates to control the voltage at bus 5 after the transient. In summary, the MPC algorithm is capable of steering the microgrid system towards a new steady-state scenario. Abrupt load shedding does not interfere with the capabilities of the MPC controller, and in both scenarios the controller managed to update the manipulated variables to reach the user-defined reference.

5.2. Test 2 - Islanding Scenario with Multiple DERs and Recursive Feasibility

Similarly to the previous section, this section is organized into three parts. The first describes the purpose and scope of the test; the second describes the operating conditions and constraints; and the third presents the analysis of the results of the microgrid operation with multiple DERs.

5.2.1. Motivation and Scope

Test 2 builds on the previous example, showcasing the MPC capabilities in both operation modes Ⓐ and Ⓑ.

The goal of this test is to illustrate the capability of the MPC architecture to concurrently steer multiple DERs in a microgrid and meet the control objectives. To this end, all components in the model in Fig. 3 are enabled,

[3]Because the system is built with phasor-domain components, voltages and currents are not represented in their sinusoidal form, rather being represented by a phasor, which has magnitude and angle. Thus, angle values are referenced against the infinite source model (the **IB** component in Fig. 3).

i.e., the test includes the conventional synchronous generator, a PV system, and a BESS unit. The primary objective is to validate the MPC algorithm for a microgrid equipped with energy sources capable of providing rapid ancillary services for frequency and voltage regulation. In addition, this test aims to illustrate that maintaining adequate system operation and feasibility does not require load shedding. Moreover, in this test the MPC has to steer the system when a sudden variation in energy production from the PV system occurs.

In summary, the purpose of Test 2 is to demonstrate the system's ability to handle fast changes in active power injection from the PV system, manage stochastic variations in both microgrid load and PV power, and undergo recursive feasibility checks.

5.2.2. Operating Conditions and Constraints

Test 2 presents two simulation scenarios, reflecting two distinct dispatch scenarios. Both include stochastic load variations, similar to Test 1. In addition, to mimic slow-varying load variations, a sinusoidal active power profile is used to modulate the load and represents the electrical load trend throughout the day.

As mentioned in Section 3.2, the WECC-based PV model (Appendix E), originally designed for transient stability analysis with a 30-second time window, was modified to account for irradiance to power conversion (as mentioned in Section 3.1). This add-on to the original model is capable of representing solar irradiance levels and stochasticity. Meanwhile, the stochastic behavior of irradiance on the active power output of the PV is modeled as proposed in (73). Approximately 99% of the time, irradiance fluctuations fall within $0\% \leq \Delta Irr \leq 3\%$ over a 1-second time frame, where ΔIrr is the increase in the output power of PV due to irradiance. Therefore, the active power injected by the PV includes a noise component that is added to the irradiance to power function, with standard deviation $\delta = 0.0001$ and a sample period of 1 second. No measurement noise was included in the experiment. For the prediction horizon and control horizon selected for the optimization stage, a value of $n_p = 20$ and $n_c = 4$ were chosen respectively. The average calculation times for the Kalman Filter and MPC Optimization stages were 0.0059 s, and 0.0067 s respectively, with a standard deviation of $\sigma = 0.0012$ s, and $\sigma = 0.0072$ s respectively.

Table 3 presents the power dispatch before islanding, showcasing two distinct simulation scenarios, referred to as "Layout". Layout 1 and Layout 2 start with the BESS charging at a rate of 1 MWh, hence the negative initial power of $P_{BESS} = -1$ MW. For Test 2, the battery's initial state of charge is defined as 50%. By initially having the BESS charged half-way, the MPC algorithm can utilize the battery for power balance ancillary services by charging and/or discharging.

Finally, in Table 4, the irradiance levels (excluding additional noise) for the two layouts are outlined, covering a 60-second simulation window. Additionally, Table 5 provides details on the constraints of the manipulated variables of the DERs. Observe that because this test takes advantage of the ancillary service capabilities of the renewable sources in the microgrid, the rate of change for G2 can be less aggressive than that applied in Test 1.

Table 3: Test 2 dispatch scenarios.

Pre-islanding steady-state scenarios [MW/MVar]								
Layout	*G1*	*G2*	*PV*	*BESS*	*Inf*	*Load 1*	*Load 2*	P_{45} *&* Q_{45}
1	53.06	5.00	2.00	-1.00	0	50.00	9.00	3.00
	7.25	0.37	0.88	1.21	14.87	10.00	2.95	0.55
2	47.05	7.00	2.00	-1.00	0	50.00	5.00	-3.00
	5.91	-0.21	0.58	0.91	13.61	10.00	1.64	0.50

Note: P_{45} and Q_{45} denote the active and reactive power flowing through the power line connecting **Bus 4**, and **Bus 5**, respectively. A positive value indicates that the microgrid imports power, while a negative value indicates that the microgrid exports power.

Table 4: Test 2 solar irradiance levels.

Irradiance Levels for 60s Simulation [kW/m^2]			
Layout	$0 \leq t < 20$ [s]	$20 \leq t < 40$ [s]	$40 \leq t \leq 60$ [s]
1	666.67	333.34	833.34
2	666.67	333.34	0

Table 5: Test 2 constraints.

MPC Manipulated Variable Constraints		
DER	*Hard Constraints*	*Soft Constraints*
G2	$2 \leq P_{ref}^{m} \leq 10$ [MW]	$-100 \leq \Delta P_{ref}^{m} \leq 100$ [kW]
	$0 \leq E_{ref}^{AVR} \leq 5$ [p.u.]	$-0.25 \leq \Delta E_{ref}^{m} \leq 0.25$ [p.u.]
PV	$-3 \leq Q_{ref}^{PV} \leq 3$ [MVar]	-
BESS	$-5 \leq P_{ref}^{BESS} \leq 5$ [MW]	-
	$-5 \leq Q_{ref}^{PV} \leq 5$ [MVar]	

5.2.3. Results

Figure 9 and 10 illustrate the recursive feasibility check of the MPC optimization process for the output variables V_{Bus5}, θ_5 and f throughout the simulation. The blue and red traces in these figures show that, due to the ability of the MPC to take advantage of the capabilities of renewable sources and their ancillary services, the output variables are well within the feasible operation region (highlighted in red) for the two "layouts" considered. The

location of the starting and end points of the trajectory in Figs. 9 and 10 indicates that, despite the perturbations, the MPC tracks the output variables to the specified reference values of $V_{Bus5} = 1$ p.u., $\theta_5 = 0°$, and $f = 60$ Hz successfully.

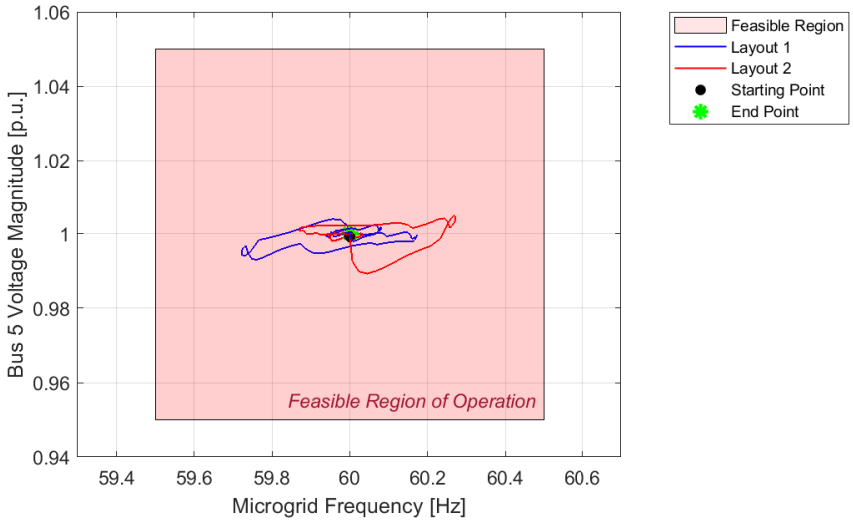

Figure 9: Bus 5 voltage magnitude and frequency feasibility region for Test 2.

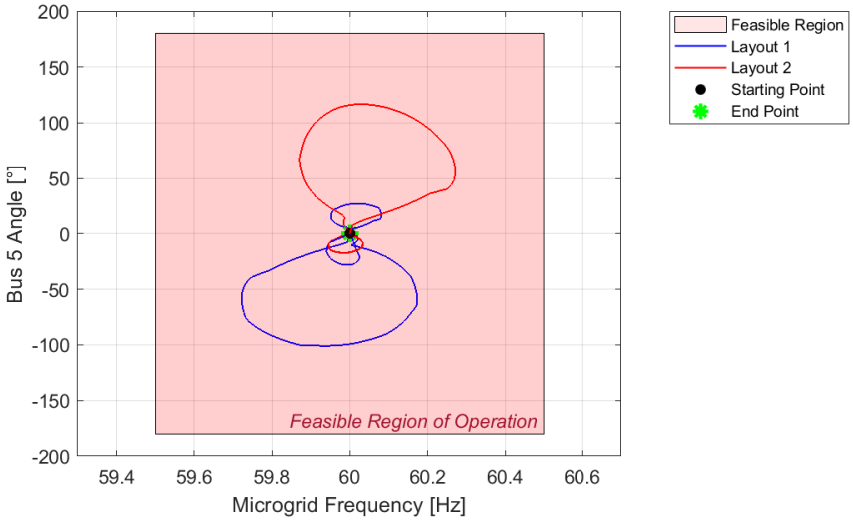

Figure 10: Bus 5 angle and frequency feasibility region for Test 2.

Figures 11 and 12 present the trajectories of the manipulated variables and output variables, respectively, which are analyzed next. Recall that in Layout 1 (see Table 3) the microgrid imports active power from the utility

grid; therefore, the BESS has to inject power to balance the load's demand after the islanding event as shown in Fig. 11 (d). This explains why the BESS's state of charge (SOC) decreases throughout the simulation as shown in Fig. 12 (e). In Layout 2 the microgrid exports active power to the utility grid, thus the BESS has to increase the charging rate to balance power, as shown in Fig. 11 (d), where it is clear that the BESS absorbs active power. Thus, the SOC level in Layout 2 is increasing, as shown in Fig. 12 (e).

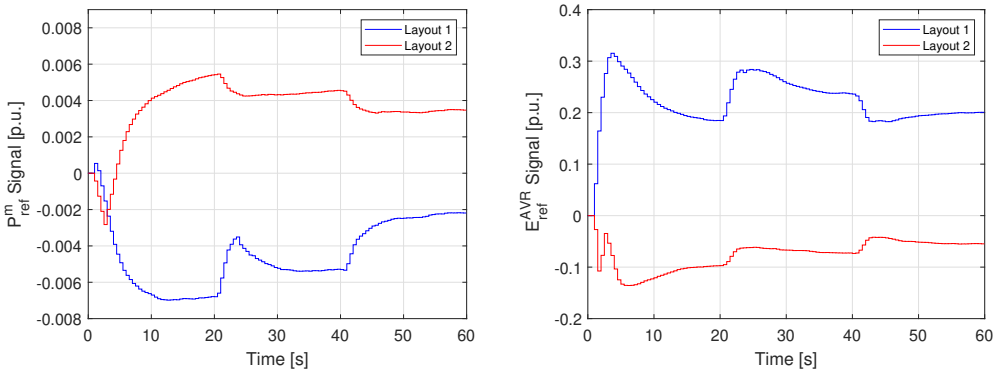

(a) P^m_{ref} input signal.

(b) E^{AVR}_{ref} input signal.

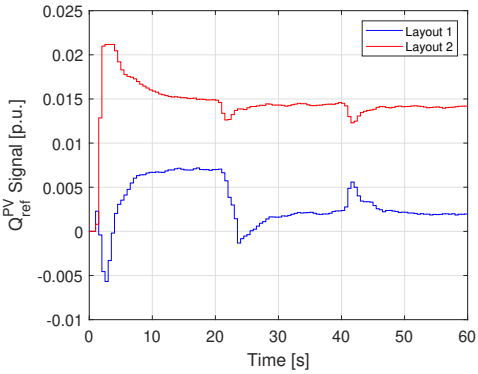

(c) Q^{PV}_{ref} input signal.

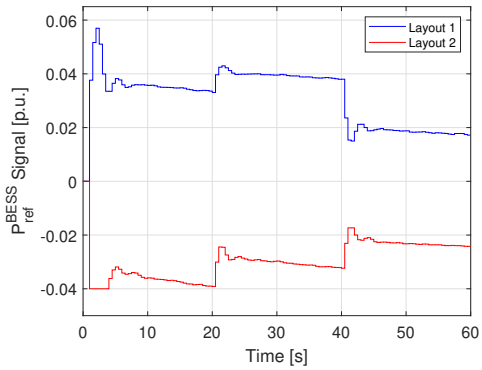

(d) P^{BESS}_{ref} input signal.

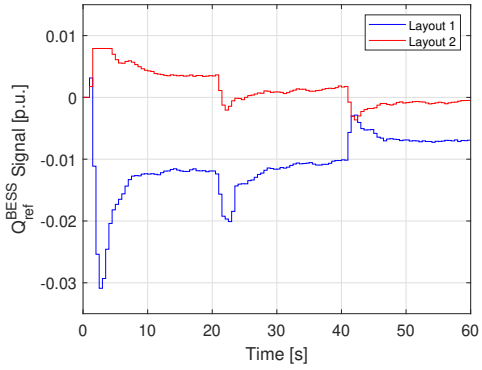

(e) Q^{BESS}_{ref} input signal.

Figure 11: MPC manipulated variables P_m^{ref}, E_m^{ref}, Q_{ref}^{PV}, P_{ref}^{BESS}, and Q_{ref}^{BESS} for Test 2.

Next, inspecting the output variables in Fig. 12, it can be observed that V_{Bus5}, θ_5, and f, are successfully controlled by the MPC by adjusting the manipulated variables (see Fig. 11).

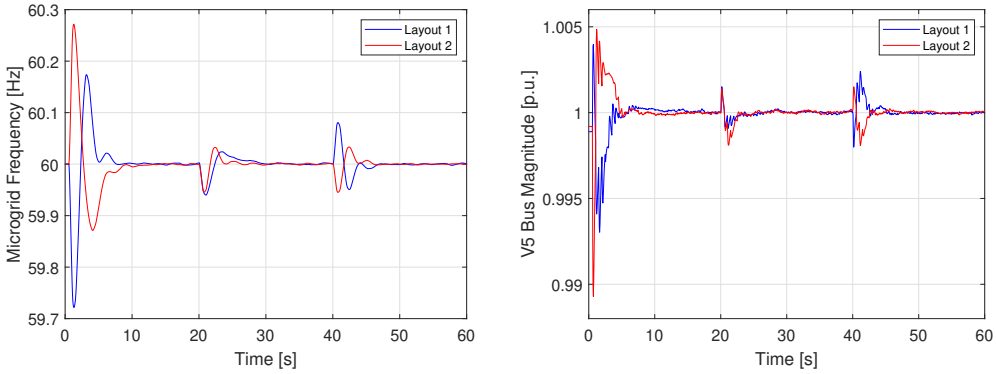

(a) Microgrid frequency.

(b) Bus 5 voltage magnitude.

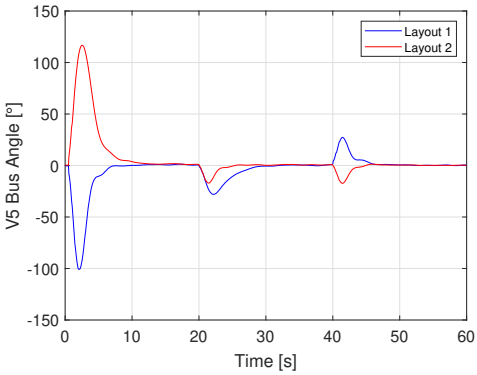

(c) Bus 5 voltage angle.

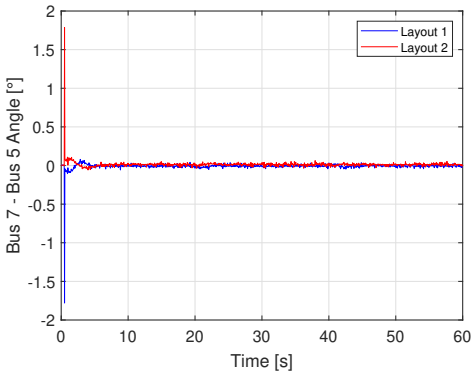

(d) Angle difference between Bus 7 and 5.

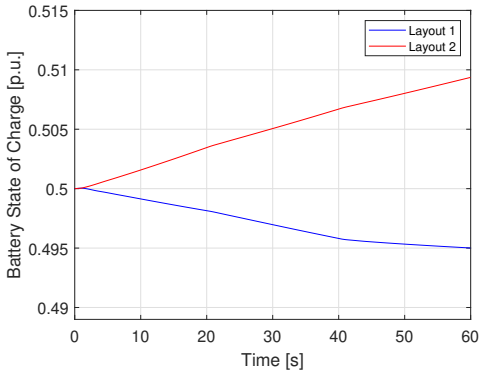

(e) BESS state of charge.

Figure 12: MPC output variable, angle difference ($\theta_7 - \theta_5$), and BESS SOC for Test 2.

Finally, it is worth noting from Fig. 12 that in both layouts, the MPC effectively steered the system to the desired values for V_{Bus5}, θ_5, and f when the system is islanded and under solar irradiance variations. Note that during islanding in Fig. 12 (d), angles in all microgrid buses lagged or led uniformly, regardless of the type of disturbance.

5.3. Test 3 - Microgrid Islanding, Autonomous Operation and Re-synchronization under Multiple DER Configurations

Similarly to the previous two tests, this section is organized in three parts. The first describes the purpose of the test; the second describes how the simulations are setup; and the third presents the results of operating the microgrid both autonomously or in grid-connected mode using the proposed MPC scheme under different DER configurations.

5.3.1. Motivation and Scope

Test 3 displays the MPC-based control performance when operating to maintain the system within system performance requirements, and also to prime the microgrid to an optimal re-synchronization. Thus, Test 3 extends the analysis from Test 2, showcasing the control capabilities of the MPC algorithm in all operation modes, i.e., Ⓐ, Ⓑ, and Ⓒ.

The goal of this test is threefold: 1) display the differences of the MPC controller in shifting the microgrid to a reference immediately after the circuit breaker trips for four different DER configuration scenarios, 2) demonstrate the capability of the MPC-based control scheme to provide flexibility by adjusting input signals to maintain the microgrid output values near a reference while having stochastic load and irradiance variations, and 3) demonstrate the capability and robustness of the MPC-based control scheme to re-synchronize the microgrid with minimal transient oscillations under the four different configuration scenarios.

5.3.2. Operating Conditions and Constraints

To illustrate the scope of the test as described above, four different system scenarios are considered:

1. **Scenario 1: G2** is the sole controllable source in the microgrid, while the **PV** and **BESS** have fixed references based on the initial pre-islanding power flow values. This implies that the only manipulated variables that are adjusted are P_m^{ref} and E_{ref}^{AVR}, while others are not updated by the MPC.
2. **Scenario 2: G2** and **PV** are controllable sources in the microgrid, while **BESS** has a fixed reference value. This implies that the manipulated variables that are adjusted include those of Scenario 1, in addition to Q_{ref}^{PV}.
3. **Scenario 3: G2** and **BESS** are the sole controllable sources in the microgrid, while **PV** has a fixed reference value. This implies that the manipulated variables that are adjusted include those of Scenario 1, in addition to P_{ref}^{BESS} and Q_{ref}^{BESS}. The initial SOC of the BESS is the same as for Test 2, with an initial charge of 50%.

4. **Scenario 4:** All DER sources in the microgrid are controllable. This implies that all manipulated variables are updated by the MPC, i.e., P_m^{ref}, E_{ref}^{AVR}, Q_{ref}^{PV}, P_{ref}^{BESS} and Q_{ref}^{BESS}. The initial SOC of the BESS is the same as for Test 2, with an initial charge of 50%.

In the simulations conducted for each of the four scenarios, the microgrid is abruptly islanded at $t = 0.55$ s, initiating the secondary control action based on MPC. In the interval of $0.55 \leq t \leq 30$ sec., the MPC-based control scheme is activated to keep $V_{Bus5} = 1$ p.u., $\theta_5 = 30°$, and $f = 60$ Hz, while the load and irradiance vary stochastically. The reason the authors chose this reference value is to show that the MPC controller is capable of transitioning from distinct operating points during the islanded operation of the microgrid. At $t = 30$ sec., the utility grid signals to the microgrid that it is ready to reconnect. All four scenarios initiate the re-synchronization phase at $t = 30$ s. During the re-synchronization phase, the output variable reference is changed to $V_{Bus5} = V_{Bus4}$ p.u., $\theta_5 = \theta_4$, and $f = 60$ Hz. This is done to minimize power oscillations during re-synchronization, as discussed in Section 2.2.

Similarly to Test 2, **Load 2** in Test 3 varies in a sinusoidal pattern with stochastic noise with standard deviation of $\delta = 0.0002$, and with a sample period of 0.02 s. The pre-islanding steady-state layout for all four different scenarios is Layout 1 from Table 3, and the constraints adopted here are the same as in Table 5. On the other hand, solar irradiance levels reflect a period of the day with low sun light variability, with an irradiance baseline of 700 [kW/m^2], and a standard deviation of $\delta = 0.002$ with a sample period of 10s. Again, no measurement noise was included in the experiment. For the prediction horizon and control horizon selected for the optimization stage, a value of $n_p = 20$ and $n_c = 4$ were chosen respectively. The average calculation times for the Kalman Filter and MPC Optimization stages were 0.0057 s, and 0.0065 s respectively, with a standard deviation of $\sigma = 0.0013$ s, and $\sigma = 0.007$ s respectively.

5.3.3. Results

Figures 13 and 14 display the feasibility check of the output variables for the four scenarios, viewed through the three output variables V_{Bus5}, θ_5, and f. Meanwhile, Figs. 15 and 16 show the manipulated variables and the output variables of interest.

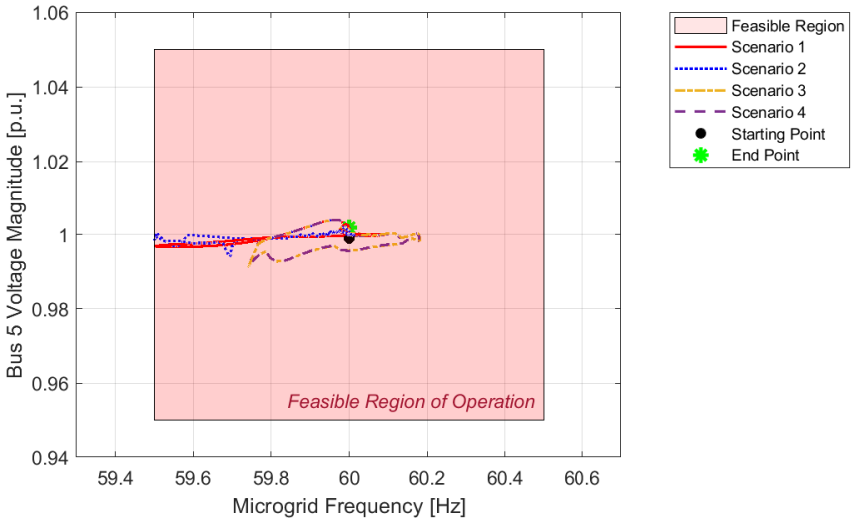

Figure 13: Bus 5 voltage magnitude and frequency feasibility region for Test 3.

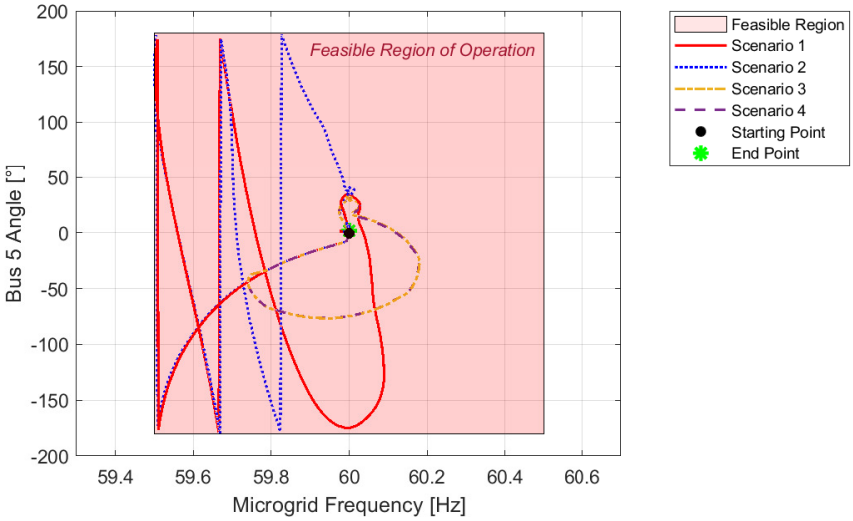

Figure 14: Bus 5 angle and frequency feasibility region for Test 3.

The feasibility graphs in Figs. 13 and 14 point to an obvious but important fact: Scenarios in which the balance of power was addressed by both **G2** and **BESS** (Scenarios 3 and 4) showed a faster return to the reference value compared to scenarios in which only **G2** controlled active power (Scenarios 1 and 2). The control over a generation unit that is capable of a fast acting ancillary service for power balance (i.e., the BESS unit) speeds up the return to the reference value. Not only that, there is also a greater feasible margin in Scenarios 3 and 4, in part due to the fast acting power balance ancillary service that the battery provides.

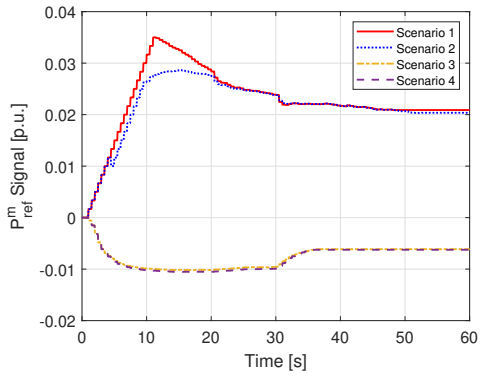

(a) P_m^{ref} input signal.

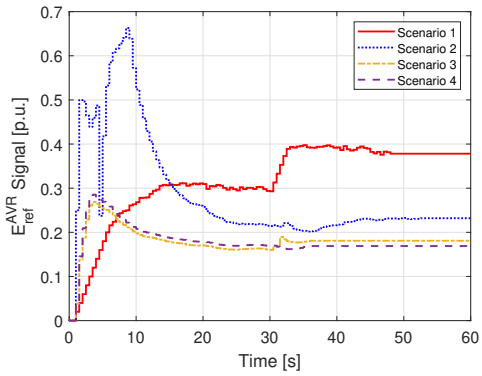

(b) E_m^{ref} input signal.

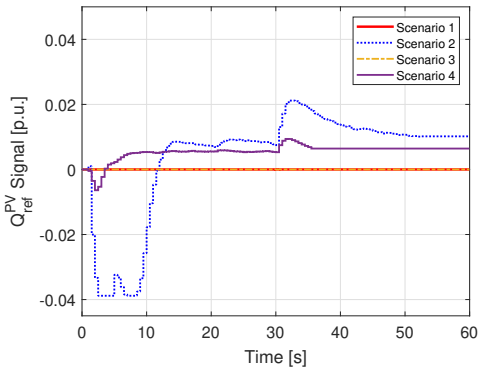

(c) Q_{ref}^{PV} input signal.

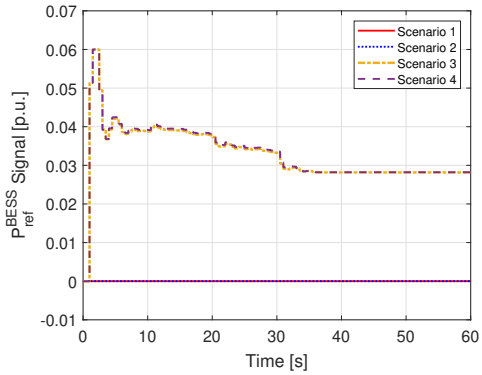

(d) P_{ref}^{BESS} input signal.

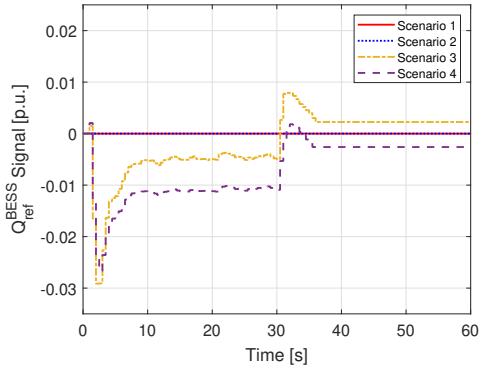

(e) Q_{ref}^{BESS} input signal.

Figure 15: MPC manipulated variables P_m^{ref}, E_m^{ref}, Q_{ref}^{PV}, P_{ref}^{BESS}, and Q_{ref}^{BESS} for Test 3.

This attribute can also be observed in Fig. 16 (a), and (c), with both f and θ_5 reaching their target reference quicker in Scenarios 3 and 4. This is true for both references, that is, from $0.55 \leq t \leq 30$ sec., where $V_{Bus5} = 1$ p.u., $\theta_5 = 30°$, and $f = 60$ Hz, and for $t > 30$ sec., where $V_{Bus5} = V_{Bus4}$ p.u., $\theta_5 = \theta_4$, and $f = 60$ Hz. Following the previous rationale, because θ_5 reaches its goal faster, $\theta_7 - \theta_5$ angle difference also stabilizes quicker, as shown in Fig.

16 (d).

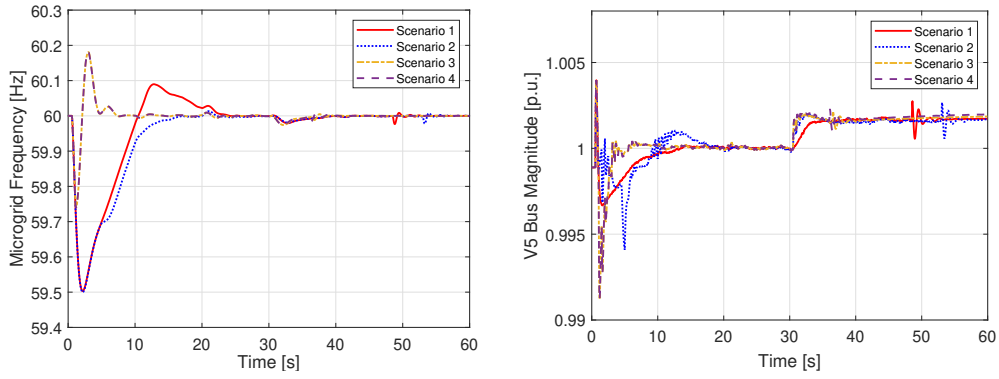

(a) Microgrid frequency.

(b) Bus 5 voltage magnitude.

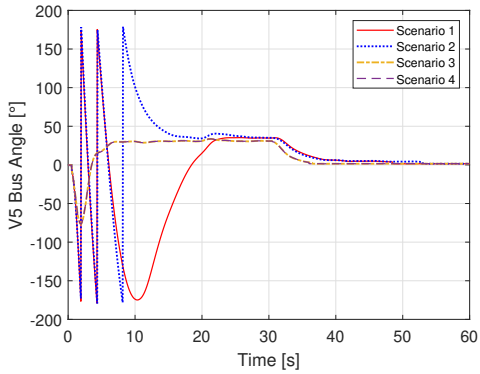

(c) Bus 5 voltage angle.

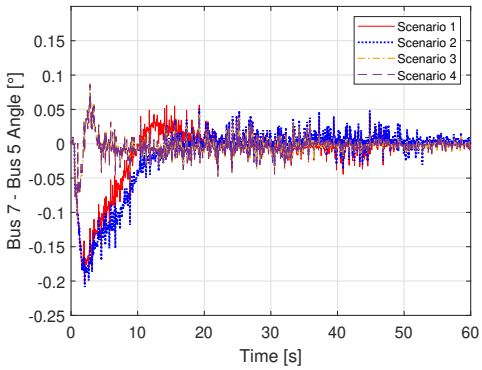

(d) Angle difference between Bus 7 and 5.

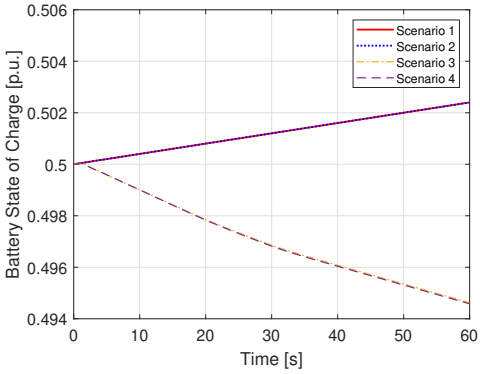

(e) BESS state of charge.

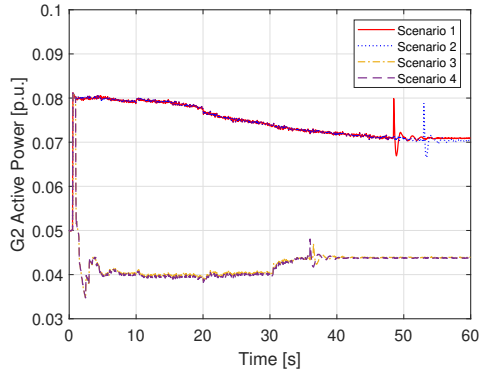

(f) G2 active power.

Figure 16: MPC output variable, angle difference ($\theta_7 - \theta_5$), BESS SOC, and G2 active power for Test 3.

The voltage magnitude in Fig. 16 (b), although it had differences in all four profiles, showed a negligible transient near the reference values during the entire simulation. Despite the differences in the controllable DERs, the four scenarios displayed fast reference tracking capabilities, as shown in Fig.

16 (b).

For the BESS's SOC, because Scenarios 1 and 2 displayed no control over BESS's manipulated variables, the battery kept charging at a rate of 1 MWh throughout the duration of the simulation, as shown in Fig. 16 (e). In Scenarios 3 and 4, where the BESS was used for power balance ancillary service, the battery discharged power, thus reducing the SOC.

The speed with which the MPC steered the microgrid towards the reference also dictates the scenarios that increase the speed of the re-synchronization process, as shown in Fig. 16 (f). Scenarios 1 and 2, relying solely on G2 for adjusting f and θ_5, result in a longer re-synchronization time. Scenario 1 took 18.35 sec. to re-synchronize the microgrid, and Scenario 2 took 22.85 sec. Scenarios 3 and 4, on the other hand, took 5.85 and 6.5 sec. to carry out the re-synchronization, respectively. Again, these results point to the fact that the BESS unit, when used for ancillary services, can improve system resilience and reliability, by speeding the re-synchronization process.

Regardless of the speed, all four scenarios had acceptable transient performance during re-synchronization, as shown in Fig. 16 (f). Scenarios 3 and 4 presented smaller transients when compared to Scenarios 1 and 2. This is due to both G2 and BESS sharing the role of actively balancing active power and frequency. All oscillation peaks during the re-synchronization process were less than 50% of their pre re-synchronization active power injection, meeting the power quality requirements defined in Section 2.2.

5.4. Test 4 - University Campus Islanding Scenario and the Impact of Communication System Delay

Similarly to the preceding three tests, this section is organized into three parts: the first part outlines the purpose of the test, the second part details the simulation setup, and the third part presents the results, focusing on the impact of communication system delays on the overall MPC controller performance. Unlike the previous tests, this evaluation is conducted using a microgrid model that emulates a real-world university campus system. For more information regarding the university microgrid system model, refer to (70).

5.4.1. Motivation and Scope

In previous test cases, the microgrid system was assumed to have no communication delays, considering only the inherent delays from Kalman Filter calculations and MPC optimization steps. However, for a real-world application like a university campus microgrid, accounting for communication system delays is crucial due to the spatial distribution of controllable sources.

The efficiency of the MPC-based algorithm relies on rapid communication systems to facilitate timely exchanges between the centralized controller

and generation units. This is crucial for accurate state estimation and updates to manipulated variables. In microgrid operations, IEEE 2030.7 is a foundational standard that specifies requirements for microgrid controllers, including maximum latency for various tasks (74). Concerning control tasks, the theoretically "ideal" maximum permissible latency is 100ms. Considering the practical constraint that achieving the ideal maximum latency might not be feasible, it raises the question: would the MPC secondary level controller exhibit sub-optimal performance as a result of delayed data exchange?

To address this inquiry, Test 4 evaluates the capability of the MPC-based secondary level controller to sustain the operational stability of the university campus microgrid during islanding (operation mode Ⓐ). The test encompasses varying levels of communication latency delay exceeding the theoretically "ideal" maximum permissible latency.

5.4.2. Operating Conditions and Constraints

A notable characteristic of this university campus microgrid is that under normal conditions, the microgrid's generation units meet 100 % of the load demand, with minimal power exchange with the grid. Although the campus has two gas and two steam turbines, it is uncommon for all four generators to operate simultaneously; typically, only two are needed to meet the load demand. Table 6 presents a power dispatch scenario for August 17, 2021, at 09:06 a.m., where only the CT1 and ST2 generation units are operational (refer to paper (70) for system layout).

Table 6: Test 4 dispatch scenarios - university campus microgrid case.

Pre-islanding steady-state scenarios [MW/MVar]													
CT1	*ST2*	*L01*	*L02*	*L03*	*L04*	*L05*	*L06*	*L07*	*L08*	*L09*	*L10*	*L11*	*PCC*
37.36	11.47	2.77	2.39	2.95	0.89	10.95	8.44	6.66	5.72	2.81	1.61	0.46	-2.3
10.91	3.441	1.12	0.34	0.59	0.04	3.35	2.02	2.18	2.22	1.02	0.56	0.24	9.05

Note: *PCC* is the point of common coupling in the university campus microgrid model. A positive value indicates that the microgrid imports power, while a negative value indicates that the microgrid exports power.

Table 7: Test 4 constraints - university campus microgrid case.

MPC Manipulated Variable Constraints		
Generation Unit	*Hard Constraints*	*Soft Constraints*
CT1	$10.78 \leq P^m_{ref} \leq 49.51$ [MW]	$-500 \leq \Delta P^m_{ref} \leq 500$ [kW]
	$-1 \leq E^{AVR}_{ref} \leq 1$ [p.u.]	$-0.25 \leq \Delta E^m_{ref} \leq 0.25$ [p.u.]
ST2	$6.40 \leq P^m_{ref} \leq 27.20$ [MW]	$-160 \leq \Delta P^m_{ref} \leq 160$ [kW]
	$-1 \leq E^{AVR}_{ref} \leq 1$ [p.u.]	$-0.25 \leq \Delta E^m_{ref} \leq 0.25$ [p.u.]

Table 7 provides details on the constraints of the generation unit manipulated variables. Loads 1 through 11 in the university campus micro-

grid include a noise component and a sinusoidal source that mimics the electrical load demand profile. The standard deviation adopted herein is $\delta = 0.0002$. The target value for the output measurements during islanding is $V_{UT02} = 1.018$ p.u., θ_{UT02} has no target value thus is free to roam, and $f = 60$ Hz. Similarly to the previous test examples, the microgrid is abruptly islanded at $t = 0.55$ s, which means that there was no time to plan ahead the pre-island power balance of the microgrid. The MPC problem was formulated with a prediction horizon $n_p = 20$, control horizon $n_c = 10$. Also, the MPC algorithm initiates the control sequence, updating the manipulated variables every 0.5 s, with a state estimation sub-tick of 0.05 s.

5.4.3. Results

Figure 17 depicts the feasibility check for output variables in four communication delay scenarios, focusing on two specific variables: the Point of Common Coupling (PCC) microgrid side voltage magnitude V_{UT02} and microgrid frequency f. The output variables never leave the feasible region of operation, pointing to the fact that the system is operating within its energy quality boundaries.

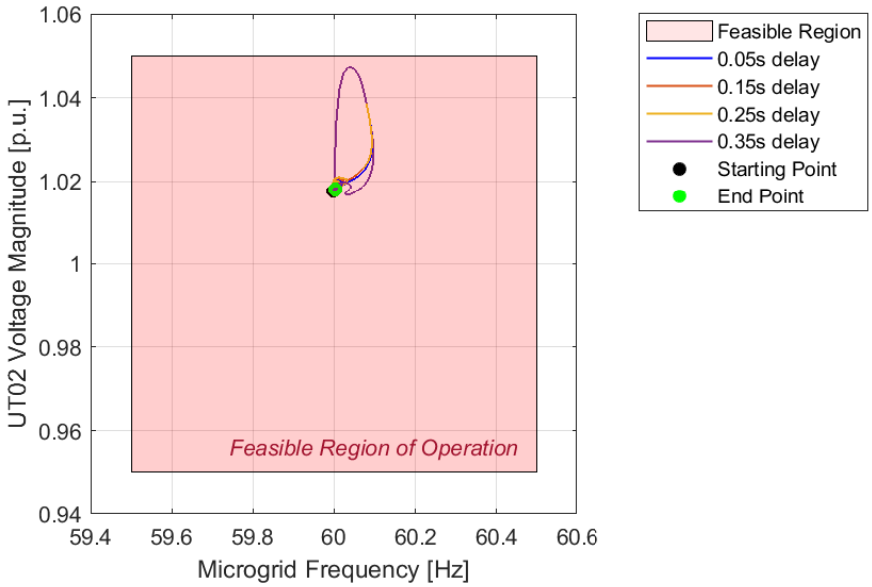

Figure 17: UT02 voltage magnitude and frequency feasibility region in test 4.

The analysis excludes the angle versus frequency plot deliberately, as the UT02 bus angle output variable is designated as a free variable, meaning it does not have a predetermined target. In systems with two or more synchronous generation units, the MPC optimization algorithm tends to adjust the active power reference in all units to simultaneously accelerate/decelerate them until the desired angle reference is achieved. Due to the gradual rate

of change in the generation units, this process is not swift, making it more appropriate to limit angle targeting to the later re-synchronization task.

Figures 18 and 19 display the manipulated variables and the output variables of interest.

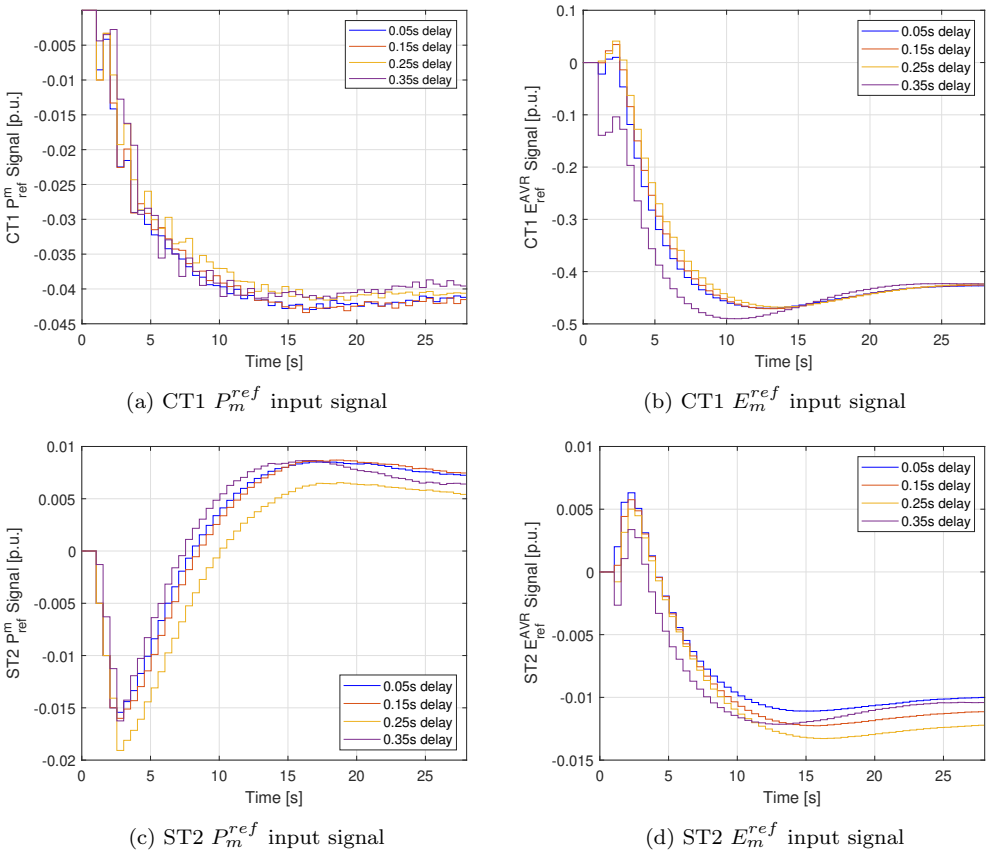

(a) CT1 P_m^{ref} input signal

(b) CT1 E_m^{ref} input signal

(c) ST2 P_m^{ref} input signal

(d) ST2 E_m^{ref} input signal

Figure 18: MPC manipulated variables CT1 P_m^{ref}, (b) CT1 E_m^{ref}, ST2 P_m^{ref}, and ST2 E_m^{ref} for Test 4.

The delay values selected for the simulations in Test 4 are 0.05s, 0.15s, 0.25s, and 0.35s. The rationale behind these four delay values is detailed below:

- **Kalman Filter Calculation:** the state estimation procedure utilizing the Kalman Filter algorithm takes on average 0.006 ± 0.0026 seconds (mean time and standard deviation).
- **MPC Optimization Calculation:** the optimization procedure for the MPC algorithm takes on average 0.0067 ± 0.0129 seconds (mean time and standard deviation).

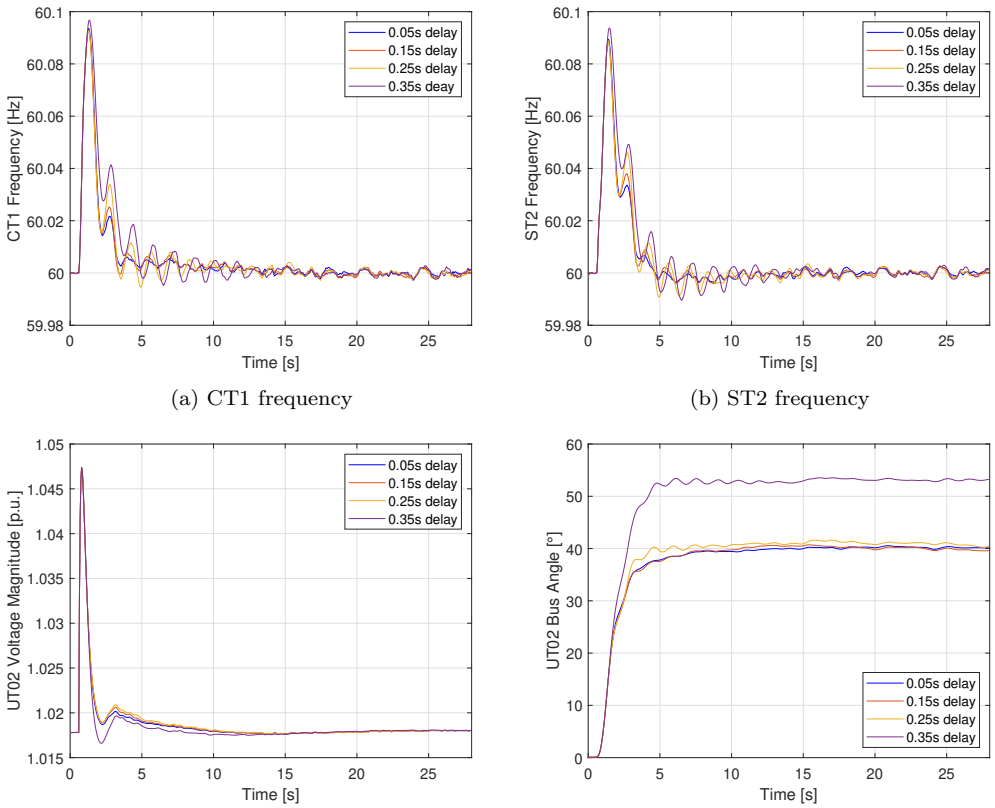

(a) CT1 frequency

(b) ST2 frequency

(c) UT02 voltage magnitude

(d) UT02 bus angle

Figure 19: MPC output variables CT1/ST2 frequency, UT02 voltage magnitude, and UT02 bus angle for Test 4.

- **Combined State Estimation and Optimization Time:** the combination of both state estimation and MPC optimization tasks result in an average delay time of (0.0127 ± 0.031) s with 95.4% certainty (total average plus two standard deviations). Thus, with 95.4% certainty, it is possible to infer that the calculation step is within one sub-tick of state estimation.

- **Total Delay Time:** the delay times of 0.15s, 0.25s, and 0.35s encompass both the time taken for calculations and the additional delay introduced by the communication system.

The introduced communication latency values, combined with the calculation delay, significantly exceed the theoretically "ideal" latency times necessary for data transmission in microgrid functions. The outcomes presented in Fig. 19 indicate that even with a larger delay of 0.35s, the MPC algorithm effectively guided the microgrid toward the predefined target, underscoring the success and efficiency of the algorithm.

5.5. Test 5 - Comparison Between PI-based Frequency Regulator and MPC Secondary Controller

Test 5 aims to contrast the simulation outcomes of the frequency regulator with those of the MPC secondary level controller, applied to the university campus microgrid model. The state-of-the-art re-synchronizer method is based on the controller defined in (75). Similarly to Test 4, Test 5 utilizes the university campus microgrid model (70). This comparison is intended to highlight the strengths and weaknesses of each formulation, providing insights into why the MPC proves to be a superior controller for secondary control schemes. In this specific comparative simulation, the assessment of both controllers will be based on their performance during operation modes Ⓐ and Ⓑ (as defined in section 2).

5.5.1. Operating Conditions and Constraints

For Test 5, the pre-islanding data utilized corresponds to the dispatch scenario detailed in Test 4. The same constraints are maintained, and the load profile remains consistent across Loads 1 through 11. However, the contingency scenario is modified, involving a sudden microgrid islanding at $t = 0.55$ s and a loss of Load 6 at $t = 23$ s, resulting in a microgrid load reduction demand of 8.44 MW and 2.02 MVar. Two simulations are conducted: one with the secondary-level MPC controller and the other with the PI frequency regulator. The leader-follower frequency regulator is applied to the largest operating generation unit (CT1 generator).

To ensure a fair comparison, the PI controller of the frequency regulator is initially tuned using the closed-loop Ziegler & Nichols method. After establishing the base tuning parameters, the author reduces the proportional gain K_p of the PI controller to minimize output oscillations resulting from the method. The final values for the gains are $K_p = 0.36$ and $K_i = 0.97$. Lastly, the delay time assumed in the MPC formulation is set at 0.25 s. For the optimization stage, the MPC problem was formulated with a prediction horizon $n_p = 20$, and control horizon $n_c = 10$.

5.5.2. Results

Figure 20 shows output variables that are comparable between simulations. Since the PI-based frequency regulator does not generate iterative manipulated variables, the simulation results from the MPC simulation are omitted. Initially, both controllers demonstrate the capability to restore the microgrid system to 60 Hz in both instances. However, the MPC-based secondary level controller stands out due to its effective mitigation of transient output oscillations, a phenomenon observed in its PI frequency regulator counterpart. In Figures 20 (a), (b), (c), and (d), the MPC-based controller exhibits less oscillatory behavior compared to the PI frequency regulator, with the added advantage of achieving nominal frequency post-event more

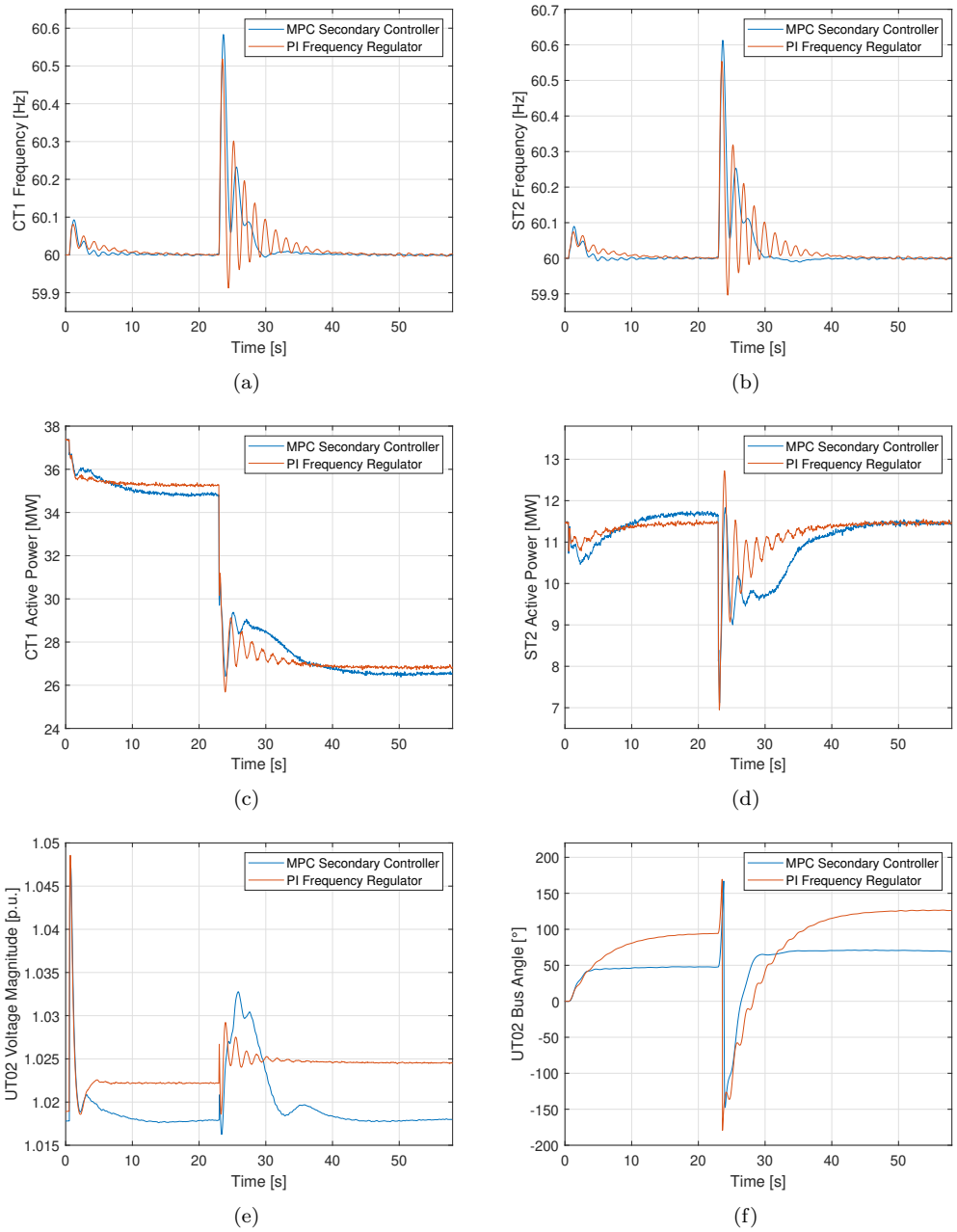

Figure 20: MPC output variable for test 2 comparison: (a) CT1 frequencies; (b) ST2 frequencies; (c) CT1 active power injections ; (d) ST2 active power injections; (e) UT02 voltage magnitudes; (f) UT02 bus angles.

swiftly. The stabilization of the microgrid's PCC bus angle (UT02 angle in Fig. 20 (f)) is achieved more rapidly with the MPC algorithm. This, in turn, is closely connected to the faster stabilization of the frequency in the MPC case as well.

A significant difference between the two methods lies in the absence of voltage magnitude control in the PI-based frequency regulator. The lack of a voltage magnitude control loop leads to an increase in voltage magnitude, shown in Fig. 20 (e)). In contrast, the MPC is capable of compelling the voltage magnitude at bus UT02 back to its pre-islanding value.

5.6. Test 6 - Re-synchronization Comparison Between MPC Secondary Controller and the Patented Re-synchronizer Controller

5.6.1. Motivation and Scope

Test 6 compares the re-synchronization outcomes between the MPC secondary level controller and the patented re-synchronization method detailed in (76), using the university campus microgrid system model (70). The comparison focuses on three key attributes: the time required for re-synchronization after signaling, the transient active power peak in the generators at re-synchronization, and the presence of significant oscillations during the process.

5.6.2. Operating Conditions and Constraints

Again, the Test 6 simulation initial condition is the same as the two previous tests. The microgrid is islanded at $t = 0.55$s, and only at $t = 28$s is when the re-synchronization action takes place in both controllers. The hard and soft constraints are also the same as previous two simulations. For the optimization stage, the MPC problem was formulated with a prediction horizon $n_p = 20$, and control horizon $n_c = 10$.

5.6.3. Results

Figure 21 displays the output comparison results from the MPC-based controller and the patented re-synchronization algorithm.

To ensure identical initial conditions for both re-synchronization methods, the initial 28 seconds of the simulation are conducted using the MPC-based controller. At $t = 28\ s$ (indicated by the $\star$ symbol), a re-synchronization signal is triggered, comparing the MPC-based re-synchronization with the patented PI-based re-synchronizer. During the initial 28 seconds, both generators stabilize voltage magnitude and frequency. Unlike previous simulations involving multiple generation units, this scenario focuses on a single controllable energy source. Controlling both generators to align the UT02 bus angle with the grid-side PCC bus angle proved slow, so the MPC-based algorithm controls only the largest energy unit, the CT1 gas turbine. The PI controller gains for the patented re-synchronizer were tuned to minimize power oscillations and achieve re-synchronization timing comparable to the MPC algorithm.

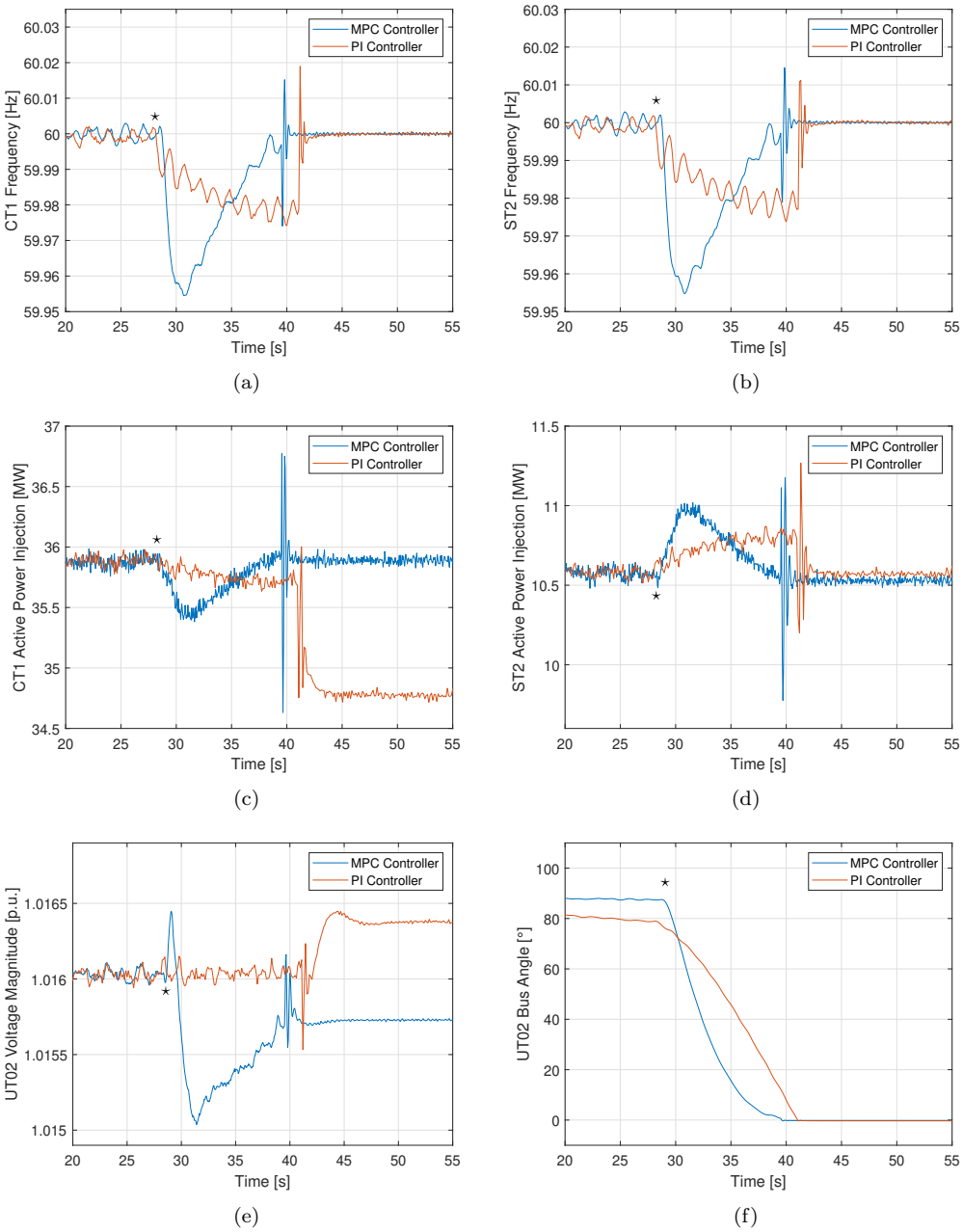

Figure 21: MPC output variable for test 3 comparison: (a) CT1 frequencies; (b) ST2 frequencies; (c) CT1 active power injections ; (d) ST2 active power injections; (e) UT02 voltage magnitudes; (f) UT02 bus angles.

A key difference between the two approaches lies in the adaptability of the PI controller, which allows users to adjust the proportional and integrator gains to induce overshoot in output variables. With minimal frequency variation, this enables the circuit breaker to quickly reconnect the microgrid

to the main grid once the controlled angle reaches a predefined value, as demonstrated in Fig. 21 (b), (d), and (f). In contrast, the MPC continuously updates input variables to minimize a cost function, achieving optimal system states when the targeted angle value is reached. While the MPC seeks an optimal combination of manipulated variable values, the primary objective of the PI controller is to reduce feedback error. The PI controller's ability to quickly bring system states near the target, even without maintaining that target, highlights an advantage of the patented method (76). The MPC-based secondary-level controller, however, was roughly 2 seconds faster on the re-synchronization task (MPC controller re-synchronized at $t = 40\ s$ while patented method at $t = 41.84\ s$), and with almost no steady-state active power deviation (comparing pre re-synchronization to post re-synchronization active power injection values for CT1 and ST2 units).

Nevertheless, based on the comprehensive simulation results, the MPC-based secondary-level controller demonstrates significant promise and viability for managing islanded microgrids. The primary advantage of the MPC controller lies in its all-in-one nature: it can track various targets depending on the microgrid's status while incorporating system constraints directly into the optimizer. This integrated approach offers a modular approach to the stability of islanded microgrids when compared to the traditional control methods currently employed in microgrids.

6. Conclusion

This paper proposes an MPC-based microgrid control scheme that provides secondary-level control functions for islanded operation and resynchronization capabilities. Multiple tests demonstrated its potential to regulate the microgrid to specified voltage magnitude, angle, and frequency levels. The proposed MPC-based control scheme can estimate the states of the microgrid system in advance using a linearized model of the non-linear system. Simulation results indicate that the scheme effectively meets the realistic physical constraints of the microgrid's distributed energy resources (DER) and can adjust tracked measurement values to predefined references, mitigating transients, especially those related to high resynchronization generator torques. Additionally, the MPC-based secondary-level controller can tolerate communication system delays while maintaining microgrid operation during islanding conditions.

The MPC-friendly microgrid simulation and optimization framework proposed by combining Dymola software with MATLAB and its Model Predictive Control Toolbox has proven effective in evaluating the proposed MPC-based control scheme. This is largely due to the reusability of the "testbed" model developed for this work that takes advantage of the object-oriented OpenIPSL Modelica library. This model provides an attractive option that

facilitates proof-of-concept studies involving MPC-based control strategies given its inherent differential and algebraic equation modeling approach, which combined with the Dymola software, can easily be used to perform dynamic simulations and derive linearized models. This is a tremendous benefit when trying to exploit existing MPC tools, such as those provided by the Model Predictive Control Toolbox in MATLAB.

Future work includes expanding the proposed method to microgrids containing multiple energy domains, such as thermal and electrical. Additionally, the authors propose expanding the MPC-based secondary control to improve resiliency of a real campus microgrid, described in (77).

Acknowledgement

This paper is based upon work supported by the U.S. Department of Energy's Office of Energy Efficiency and Renewable Energy (EERE) under the Advanced Manufacturing Office, Award Number DE-EE0009139, and in part by the National Science Foundation Award No. 2231677.

This paper was prepared as an account of work sponsored by an agency of the United States Government. Neither the United States Government nor any agency thereof, nor any of their employees, makes any warranty, express or implied, or assumes any legal liability or responsibility for the accuracy, completeness, or usefulness of any information, apparatus, product, or process disclosed, or represents that its use would not infringe privately owned rights. Reference herein to any specific commercial product, process, or service by trade name, trademark, manufacturer, or otherwise does not necessarily constitute or imply its endorsement, recommendation, or favoring by the United States Government or any agency thereof. The views and opinions of authors expressed herein do not necessarily state or reflect those of the United States Government or any agency thereof.

Appendix A. MPC-based Secondary Control and Re-synchronization Flowchart

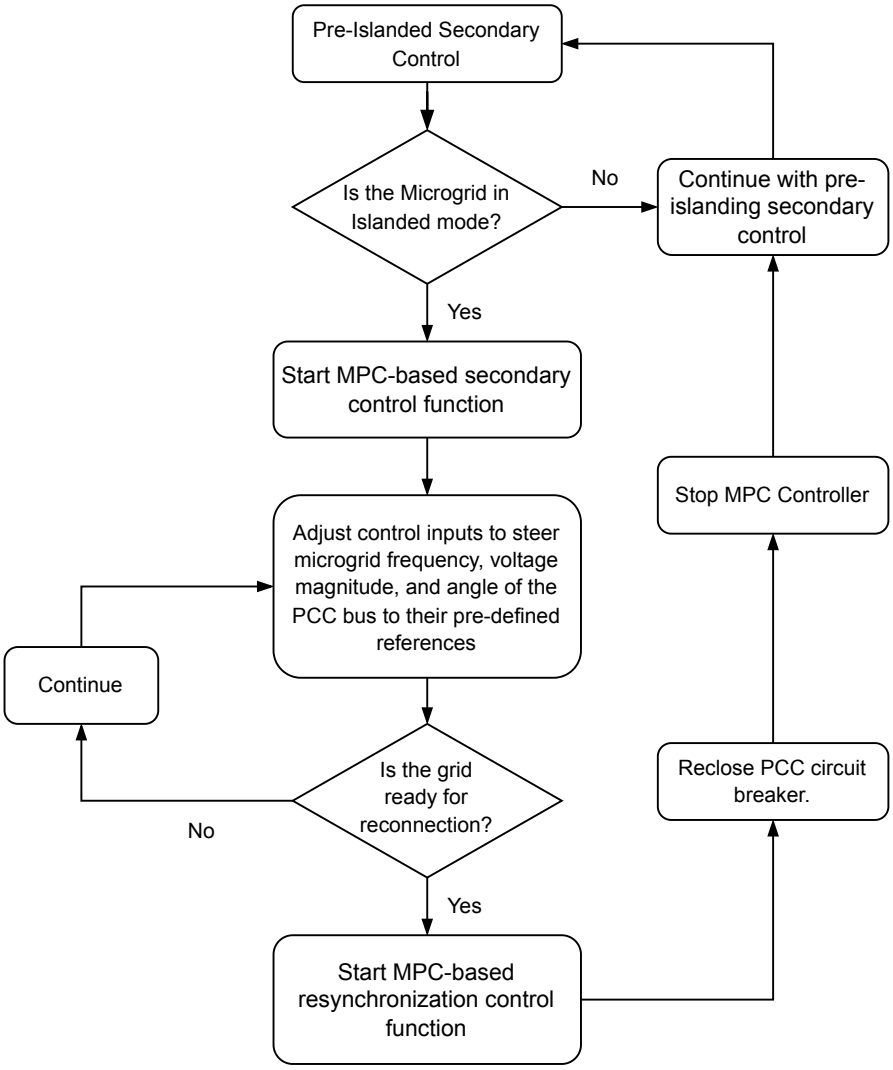

Appendix B. Overall Implementation Procedure of the Secondary Level MPC Control Simulation Environment

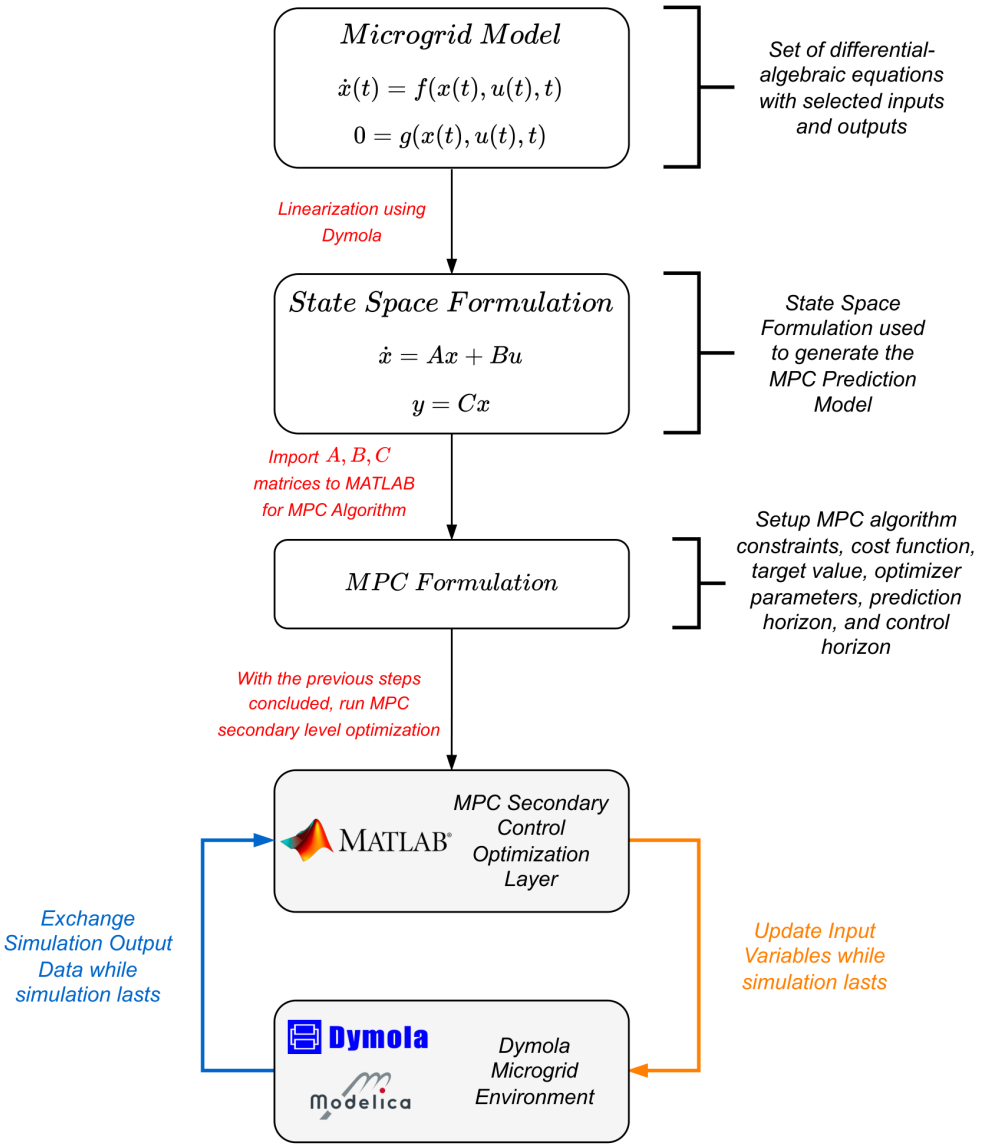

Appendix C. GAST Gas Turbine Governor Block Diagram

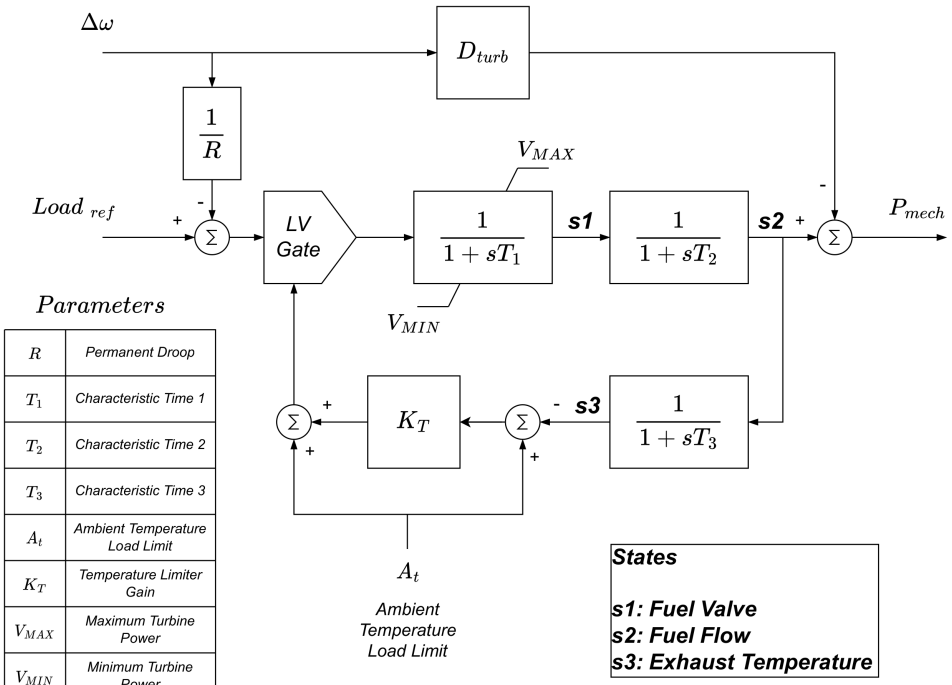

Parameters

R	*Permanent Droop*
T_1	*Characteristic Time 1*
T_2	*Characteristic Time 2*
T_3	*Characteristic Time 3*
A_t	*Ambient Temperature Load Limit*
K_T	*Temperature Limiter Gain*
V_{MAX}	*Maximum Turbine Power*
V_{MIN}	*Minimum Turbine Power*
D_{turb}	*Turbine Damping Coefficient*

Appendix D. SEXS Exciter Block Diagram

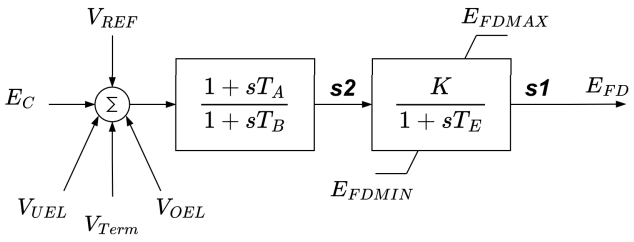

Parameters

T_A	*Lead Time Constant*
T_B	*Lag Time Constant*
K	*Voltage Regulator Gain*
T_E	*Exciter field time constant*
E_{FDMIN}	*Minimum excitation output*
E_{FDMAX}	*Maximum excitation output*

States

s1: Excitation Voltage
s2: Lead-Lag

Appendix E. PV Block Diagram

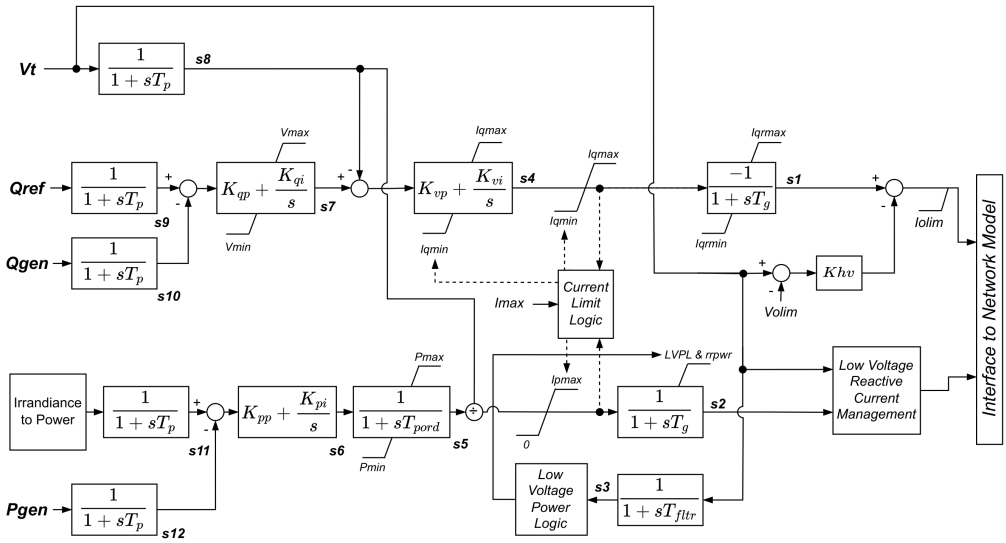

Parameters

T_P	*Sensor Time Constant*	K_{pp}	*P Regulator Proportional Gain*
T_{pord}	*Power Filter Time Constant*	K_{pi}	*P Regulator Integral Gain*
T_{fltr}	*Voltage Filter Time Constant*	P_{PV}	*PV Output Power*
T_g	*Converter Time Constant*	Y_{PV}	*Rated Capacity of the PV Array*
Khv	*Overvoltage Compensation Gain*	f_{PV}	*PV Derating Factor*
K_{qp}	*Q Regulator Proportional Gain*	$\bar{G}_T$	*Solar Irradiance on the PV*
K_{qi}	*Q Regulator Integral Gain*	$\bar{G}_{T,STC}$	*Incident Radiation at Standard Test Conditions*
K_{vp}	*V Regulator Proportional Gain*	α_P	*Temperature Coefficient of Power*
K_{vi}	*V Regulator Integral Gain*	$(T_c - T_{c,STC})$	*PV Cell Temperature Difference*

Irradiance to Power

$$P_{PV} = Y_{PV} f_{PV} \left(\frac{\bar{G}_T}{\bar{G}_{T,STC}} \right) \left[1 + \alpha_P \left(T_c - T_{c,STC} \right) \right]$$

States

s1: Converter lag for Iq
s2: Converter lag for Ip
s3: Voltage filter
s4: PI Controller for V error
s5: First Order Lag for Tpord
s6: PI Controller for P error
s7: PI Controller for Q errr
s8: Voltage Measurement Filter
s9: Q Reference Signal Delay
s10: Q Measurement Filter
s11: P Reference Signal Delay
s12: P Measurement Filter

Appendix F. BESS Block Diagram

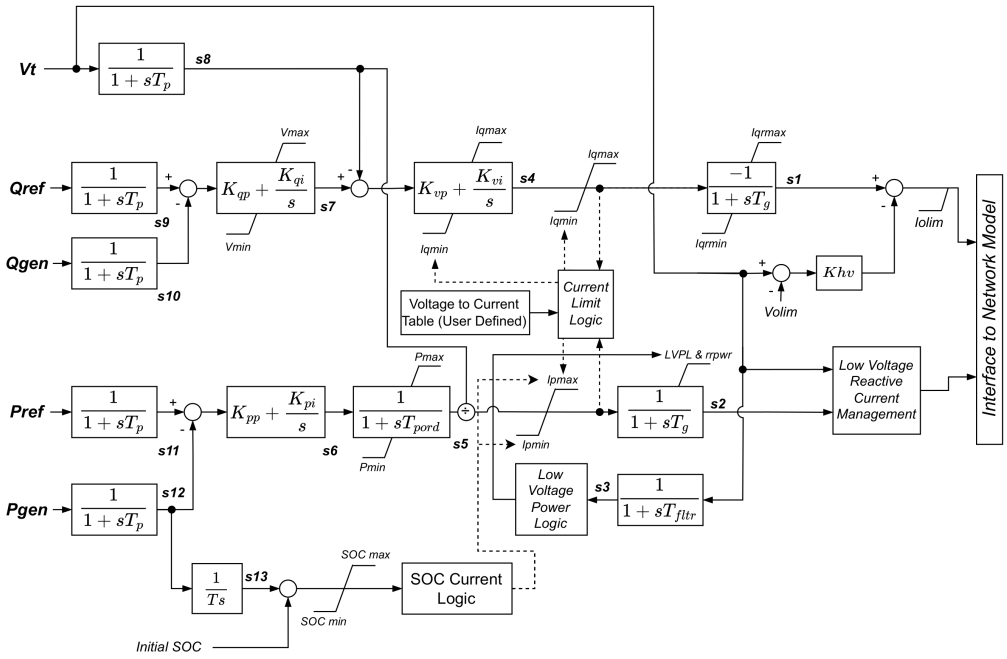

Parameters

T_P	*Sensor Time Constant*	K_{qi}	*Q Regulator Integral Gain*
T_{pord}	*Power Filter Time Constant*	K_{vp}	*V Regulator Proportional Gain*
T_{fltr}	*Voltage Filter Time Constant*	K_{vi}	*V Regulator Integral Gain*
T_g	*Converter Time Constant*	K_{pp}	*P Regulator Proportional Gain*
Khv	*Overvoltage Compensation Gain*	K_{pi}	*P Regulator Integral Gain*
K_{qp}	*Q Regulator Proportional Gain*	T	Battery Discharge Time in seconds

States

s1: Converter lag for Iq
s2: Converter lag for Ip
s3: Voltage filter
s4: PI Controller for V error
s5: First Order Lag for Tpord
s6: PI Controller for P error
s7: PI Controller for Q errr
s8: Voltage Measurement Filter
s9: Q Reference Signal Delay
s10: Q Measurement Filter
s11: P Reference Signal Delay
s12: P Measurement Filter
s13: Battery State of Charge (SOC)

Appendix G. Reduced Order PV/BESS Block Diagram

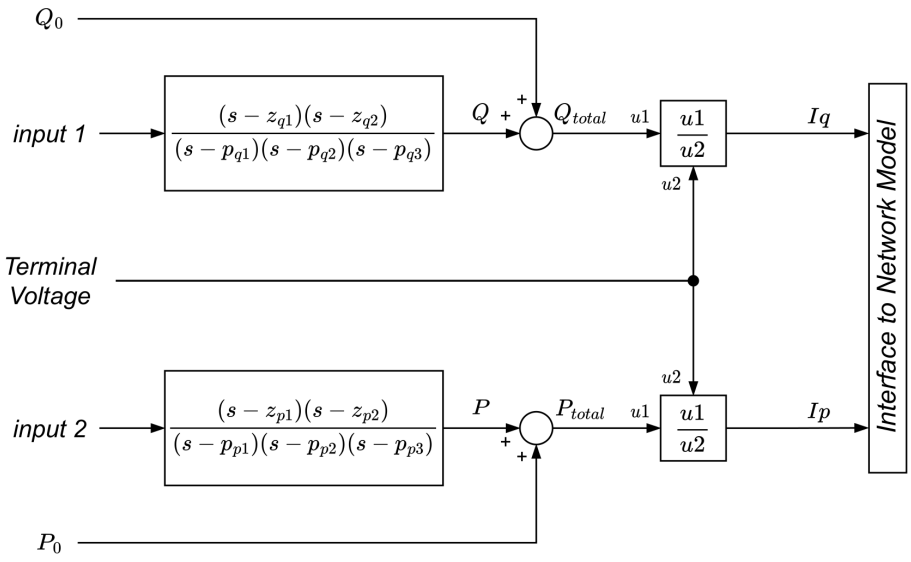

Appendix H. Energy Source Parameters

Component	Parameter	Value	Unit
IB	Machine Base	100	MVA
	Inertia	0	s
	Damping	0	p.u.
	Armature Resistance	0	p.u.
	d-axis Reactance	1	p.u.
G1 GENSAL	Base Voltage	6	kV
	Machine Base	100	MVA
	d-axis Transient Open Circuit Time Constant	5	s
	d-axis Sub-transient Open Circuit Time Constant	0.07	s
	q-axis Sub-transient Open Circuit Time Constant	0.09	s
	Inertia	3.28	s
	Speed Damping	1	-
	d-axis Reactance	1.84	p.u.
	q-axis Reactance	1.75	p.u.
	d-axis Transient Reactance	0.41	p.u.
	d-axis Sub-transient Reactance	0.2	p.u.
	q-axis Sub-transient Reactance	0.2	p.u.
	Leakage Reactance	0.12	p.u.
	Saturation Factor at 1.0 p.u.	0.11	p.u.
	Saturation Factor at 1.2 p.u.	0.39	p.u.
	Armature Resistance	0	p.u.
G1 HYGOV	Permanent Droop Gain	0.05	p.u.
	Temporary Droop Gain	0.3	p.u.
	Governor Time Constant	5	s
	Filter Time Constant	0.05	s
	Servo Time Constant	0.5	s
	Gate Open/Close Velocity Limit	0.2	1/s
	Maximum Gate Limit	0.9	p.u.
	Minimum Gate Limit	0	p.u.
	Water Time Constant	1.25	s
	Turbine Gain	1.2	p.u.
	Turbine Damping	0.2	p.u.
	Water Flow at no Load	0.08	p.u.
	Water Head Initial Value	1	p.u.
G1 SEXS	Lead Time Constant	0.1	s
	Lag Time Constant	1	s
	Excitation Power Source Output Gain	100	-
	Excitation Power Source Output Time Constant	0.1	s
	Minimum Exciter Output	-10	p.u.
	Maximum Exciter Output	10	p.u.
G2 GENROU	Base Voltage	6	kV
	Machine Base	16.667	MVA
	d-axis Transient Open Circuit Time Constant	4.822	s
	d-axis Sub-transient Open Circuit Time Constant	0.023	s
	q-axis Sub-transient Open Circuit Time Constant	0.065	s
	Inertia	8.75	s
	Speed Damping	2	-
	d-axis Reactance	1.897	p.u.
	q-axis Reactance	1.78	p.u.
	d-axis Transient Reactance	0.23	p.u.
	d-axis Sub-transient Reactance	0.156	p.u.
	q-axis Sub-transient Reactance	0.156	p.u.
	Leakage Reactance	0.123	p.u.
	Saturation Factor at 1.0 p.u.	0.12	p.u.
	Saturation Factor at 1.2 p.u.	0.40	p.u.
	Armature Resistance	0	p.u.
	q-axis Transient Reactance	0.23	p.u.
	q-axis Transient Open-circuit Time Constant	4.822	s
	Sub-transient Reactance	0.156	p.u.
G2 GAST	Speed Droop Gain	0.05	p.u.
	Valve Response Time Constant	0.4	s
	Turbine Response Time Constant	0.1	s
	Load Limit Response Time Constant	3	s
	Ambient Temperature Load Limit	0.9	p.u.
	Temperature Limiter Gain	2	p.u.
	Maximum Turbine Power	1	p.u.
	Minimum Turbine Power	0.1	p.u.
	Turbine Damping	0.1	p.u.
G2 SEXS	Lead Time Constant	2	s
	Lag Time Constant	10	s
	Excitation Power Source Output Gain	50	-
	Excitation Power Source Output Time Constant	0.01	s
	Minimum Exciter Output	0	p.u.
	Maximum Exciter Output	5	p.u.

Appendix I. Energy Source Parameters (Continuation)

Component	Parameter	Value	Unit
PV and BESS	Base Voltage	480	V
	Machine Base	100	MVA
	Converter Time Constant	0.02	s
	LVPL Ramp Rate Limit	10	1/s
	LVPL Characteristic Voltage 1	0.5	p.u.
	LVPL Characteristic Voltage 2	0.9	p.u.
	LVPL gain	1.22	p.u.
	Voltage Limit for HVRC Management	1.2	p.u.
	High Voltage Point for LVAC Management	0.8	p.u.
	Low Voltage Point for LVAC Management	0.4	p.u.
	Current Limit for HVRC Management	-1.3	p.u.
	Voltage Filter Time Constant for LVAC Management	0.02	s
	Power Filter Time Constant for LVAC Management	0.05	s
	Over-Voltage Compensation Gain HVRC Management	0.7	s
	Upper Limit for Rate of Change for Reactive Current	9999	p.u./s
	Lower Limit for Rate of Change for Reactive Current	-9999	p.u./s
	Filter time constant for Voltage and Power Measurement	0.02	s
	Upper Limit on Reactive Current Injection	1.05	p.u.
	Lower Limit on Reactive Current Injection	-1.05	p.u.
	Upper Limit of Reactive Power Regulator	0.4360	p.u.
	Lower Limit of Reactive Power Regulator	-0.4360	p.u.
	Maximum Limit for Voltage Control Limit	1.1	p.u.
	Minimum Limit for Voltage Control Limit	0.9	p.u.
	Maximum Limit for Active Power Limit	1	p.u.
	Minimum Limit for Active Limit	0.001	p.u.
	Maximum Limit on Total Converter Current	1.3	p.u.
	Proportional Gain for Voltage Control	1	-
	Integral Gain for Voltage Control	0.1	-
	Proportional Gain for Reactive Power Control	1	-
	Integral Gain for Reactive Power Control	1	-
	Proportional Gain for Active Power Control	1	-
	Integral Gain for Active Power Control	1	-
BESS	Reactive Power V-I Pair, Voltage 1	0.2	p.u.
	Reactive Power V-I Pair, Current 1	0.75	p.u.
	Reactive Power V-I Pair, Voltage 2	0.5	p.u.
	Reactive Power V-I Pair, Current 2	0.75	p.u.
	Reactive Power V-I Pair, Voltage 3	0.75	p.u.
	Reactive Power V-I Pair, Current 3	0.75	p.u.
	Reactive Power V-I Pair, Voltage 4	1	p.u.
	Reactive Power V-I Pair, Current 4	0.75	p.u.
	Active Power V-I Pair, Voltage 1	0.2	p.u.
	Active Power V-I Pair, Current 1	1.11	p.u.
	Active Power V-I Pair, Voltage 2	0.5	p.u.
	Active Power V-I Pair, Current 2	1.11	p.u.
	Active Power V-I Pair, Voltage 3	0.75	p.u.
	Active Power V-I Pair, Current 3	1.11	p.u.
	Active Power V-I Pair, Voltage 4	1	p.u.
	Active Power V-I Pair, Current 4	1.11	p.u.
	Battery Charge/Discharge Time	250	s
	Initial State of Charge	0.5	p.u.
	Maximum Allowable State of Charge	0.8	p.u.
	Minimum Allowable State of Charge	0.2	p.u.

Appendix J. Electrical Grid Parameters

Component	Parameter	Value	Unit
System Data	System Base Power	100	MVA
	System Frequency	60	Hz
Bus 1	Nominal Voltage	6	kV
Bus 2	Nominal Voltage	13.8	kV
Bus 3	Nominal Voltage	13.8	kV
Bus 4	Nominal Voltage	13.8	kV
Bus 5	Nominal Voltage	13.8	kV
Bus 6	Nominal Voltage	6	kV
Bus 7	Nominal Voltage	13.8	kV
Bus 8	Nominal Voltage	0.48	kV
Bus 9	Nominal Voltage	13.8	kV
Bus 10	Nominal Voltage	0.48	kV
Bus 11	Nominal Voltage	13.8	kV
Transformer 1	Specified Resistance	0.001	p.u.
	Specified Reactance	0.2	p.u.
	Magnetizing Susceptance	0	p.u.
	Magnetizing Conductance	0	p.u.
	Voltage High Side	13.8	kV
	Voltage Low Side	6	kV
Transformer 2	Specified Resistance	0.005	p.u.
	Specified Reactance	0.1	p.u.
	Magnetizing Susceptance	0	p.u.
	Magnetizing Conductance	0	p.u.
	Voltage High Side	13.8	kV
	Voltage Low Side	6	kV
Transformer 3	Specified Resistance	0.001	p.u.
	Specified Reactance	0.1	p.u.
	Magnetizing Susceptance	0	p.u.
	Magnetizing Conductance	0	p.u.
	Voltage High Side	13.8	kV
	Voltage Low Side	0.48	kV
Transformer 4	Specified Resistance	0.001	p.u.
	Specified Reactance	0.1	p.u.
	Magnetizing Susceptance	0	p.u.
	Magnetizing Conductance	0	p.u.
	Voltage High Side	13.8	kV
	Voltage Low Side	0.48	kV
Line 1 and 3	Resistance	0.001	p.u.
	Reactance	0.2	p.u.
	Shunt Half Conductance	0	p.u.
	Shunt Half Susceptance	0	p.u.
Line 2 Upper/Bottom Line	Resistance	0.0005	p.u.
	Reactance	0.1	p.u.
	Shunt Half Conductance	0	p.u.
	Shunt Half Susceptance	0	p.u.
Line 4, 5, and 6	Resistance	0.01	p.u.
	Reactance	0.001	p.u.
	Shunt Half Conductance	0	p.u.
	Shunt Half Susceptance	0	p.u.

Appendix K. University Campus Microgrid System Schematic Diagram for MPC Application

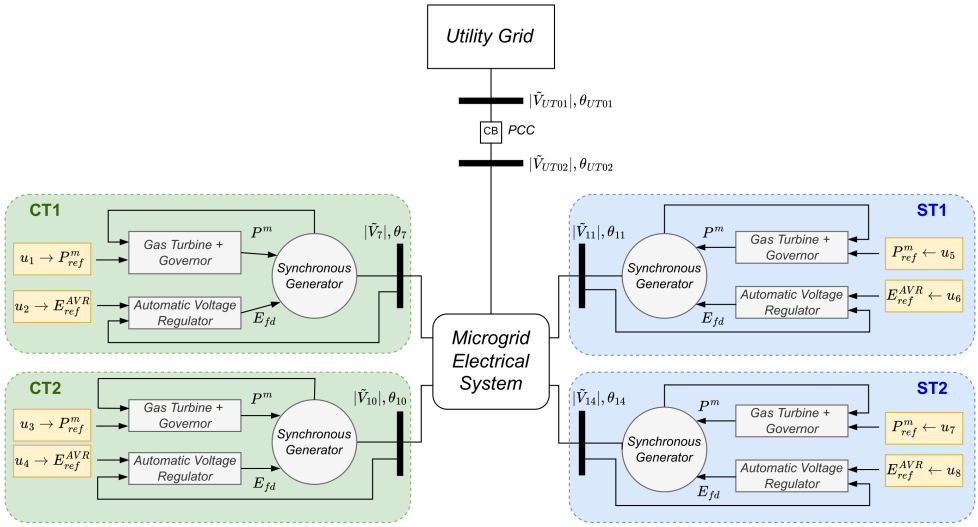

References

[1] J. J. Grainger, Power system analysis, McGraw-Hill, 1999.

[2] A. Harvey, A. Larson, S. Patel, History of power: The evolution of the electric generation industry, Power Magazine 161 (2017).

[3] M. Farrokhabadi, C. A. Canizares, J. W. Simpson-Porco, E. Nasr, L. Fan, P. A. Mendoza-Araya, R. Tonkoski, U. Tamrakar, N. Hatziargyriou, D. Lagos, et al., Microgrid stability definitions, analysis, and examples, IEEE Transactions on Power Systems 35 (1) (2019) 13–29.

[4] D. T. Ton, M. A. Smith, The US department of energy's microgrid initiative, The Electricity Journal 25 (8) (2012) 84–94. doi:10.1016/j.tej.2012.09.013.

[5] J. Surash, R. Hughes, Developing microgrids to deliver energy resilience (April 2022).
URL https://www.army.mil/article/255597/developing_microgrids_to_deliver_energy_resilience

[6] A. Lagrange, M. de Simón-Martín, A. González-Martínez, S. Bracco, E. Rosales-Asensio, Sustainable microgrids with energy storage as a means to increase power resilience in critical facilities: An application to a hospital, International Journal of Electrical Power & Energy Systems 119 (2020) 105865.

[7] L. Yu, T. Jiang, Y. Zou, Distributed real-time energy management in data center microgrids, IEEE Transactions on Smart Grid 9 (4) (2016) 3748–3762.

[8] J. Pascual, J. Barricarte, P. Sanchis, L. Marroyo, Energy management strategy for a renewable-based residential microgrid with generation and demand forecasting, Applied Energy 158 (2015) 12–25.

[9] P. Sreedharan, J. Farbes, E. Cutter, C.-K. Woo, J. Wang, Microgrid and renewable generation integration: University of california, san diego, Applied energy 169 (2016) 709–720.

[10] D. Gutiérrez-Oliva, A. Colmenar-Santos, E. Rosales-Asensio, A review of the state of the art of industrial microgrids based on renewable energy, Electronics 11 (7) (2022) 1002.

[11] G. B. Kumar, K. Palanisamy, A review of energy storage participation for ancillary services in a microgrid environment, Inventions 5 (4) (2020) 63.

[12] B. Mukherjee, M. de Castro Fernandes, L. Vanfretti, A PMU-based control scheme for islanded operation and re-synchronization of der, International Journal of Electrical Power & Energy Systems 133 (2021) 107217.

[13] M. S. Almas, L. Vanfretti, RT-HIL Implementation of the hybrid synchrophasor and GOOSE-based passive islanding schemes, IEEE Transactions on Power Delivery 31 (3) (2016) 1299–1309. doi:10.1109/TPWRD.2015.2473669.

[14] M. S. Almas, L. Vanfretti, A hybrid synchrophasor and goose-based power system synchronization scheme, IEEE Access 4 (2016) 4659–4668. doi:10.1109/ACCESS.2016.2601445.

[15] I. Serban, C. Marinescu, Control strategy of three-phase battery energy storage systems for frequency support in microgrids and with uninterrupted supply of local loads, IEEE Transactions on power electronics 29 (9) (2013) 5010–5020.

[16] D. E. Olivares, A. Mehrizi-Sani, A. H. Etemadi, C. A. Cañizares, R. Iravani, M. Kazerani, A. H. Hajimiragha, O. Gomis-Bellmunt, M. Saeedifard, R. Palma-Behnke, et al., Trends in microgrid control, IEEE Transactions on smart grid 5 (4) (2014) 1905–1919.

[17] M. Monadi, H. Hooshyar, L. Vanfretti, F. Mahmood, J. I. Candela, P. Rodriguez, Measurement-based network clustering for active distribution systems, IEEE Transactions on Smart Grid 10 (6) (2019) 6714–6723. doi:10.1109/TSG.2019.2910510.

[18] K. P. Silva, D. F. Casamali, A. S. e Silva, Coordinated control design for reconnection of islanded generation, Journal of Control, Automation and Electrical Systems 31 (2020) 1221–1232.

[19] T. M. L. Assis, G. N. Taranto, Automatic reconnection from intentional islanding based on remote sensing of voltage and frequency signals, IEEE Transactions on Smart Grid 3 (4) (2012) 1877–1884. doi:10.1109/TSG.2012.2191579.

[20] J. Hu, Y. Shan, J. M. Guerrero, A. Ioinovici, K. W. Chan, J. Rodriguez, Model predictive control of microgrids–an overview, Renewable and Sustainable Energy Reviews 136 (2021) 110422.

[21] Y. Khayat, Q. Shafiee, R. Heydari, M. Naderi, T. Dragičević, J. W. Simpson-Porco, F. Dörfler, M. Fathi, F. Blaabjerg, J. M. Guerrero, et al., On the secondary control architectures of ac microgrids: An overview, IEEE Transactions on Power Electronics 35 (6) (2019) 6482–6500.

[22] M. F. Zia, E. Elbouchikhi, M. Benbouzid, Microgrids energy management systems: A critical review on methods, solutions, and prospects, Applied energy 222 (2018) 1033–1055.

[23] L. Ahmethodzic, M. Music, Comprehensive review of trends in microgrid control, Renewable Energy Focus 38 (2021) 84–96.

[24] Q. Shafiee, J. M. Guerrero, J. C. Vasquez, Distributed secondary control for islanded microgrids—a novel approach, IEEE Transactions on power electronics 29 (2) (2013) 1018–1031.

[25] C. Ahumada, R. Cárdenas, D. Saez, J. M. Guerrero, Secondary control strategies for frequency restoration in islanded microgrids with consideration of communication delays, IEEE Transactions on Smart Grid 7 (3) (2015) 1430–1441.

[26] mtu Solutions, An introduction to microgrids (January 2024).
URL `https://www.mtu-solutions.com/na/en/technical-articles/2019/an-introduction-to-microgrids.html`

[27] Nyserda, Design of a resilient underground microgrid in potsdam, ny (January 2024).
URL `https://www.nyserda.ny.gov/-/media/Project/Nyserda/Files/Publications/Research/Electic-Power-Delivery/Microgrids-Report-Summary.pdf`

[28] R. C. Schaefer, Art of generator synchronizing, IEEE Transactions on Industry Applications 53 (1) (2016) 751–757.

[29] R. A. Evans, A manual/automatic synchronization circuit for a 37.5 mva steam-turbine-driven generator, IEEE Transactions on Industry Applications 26 (6) (1990) 1081–1085.

[30] C. Cho, J.-H. Jeon, J.-Y. Kim, S. Kwon, K. Park, S. Kim, Active synchronizing control of a microgrid, IEEE Transactions on Power Electronics 26 (12) (2011) 3707–3719.

[31] M. Rasheduzzaman, S. N. Bhaskara, B. H. Chowdhury, Implementation of a microgrid central controller in a laboratory microgrid network, in: 2012 North American Power Symposium (NAPS), IEEE, 2012, pp. 1–6.

[32] Y. Sun, C. Zhong, X. Hou, J. Yang, H. Han, J. M. Guerrero, Distributed cooperative synchronization strategy for multi-bus microgrids, International Journal of Electrical Power & Energy Systems 86 (2017) 18–28.

[33] J. Hu, Y. Shan, J. M. Guerrero, A. Ioinovici, K. W. Chan, J. Rodriguez, Model predictive control of microgrids – an overview, Renewable and Sustainable Energy Reviews 136 (2021) 110422. doi:https://doi.org/10.1016/j.rser.2020.110422.
URL https://www.sciencedirect.com/science/article/pii/S1364032120307097

[34] S. Vazquez, J. Rodriguez, M. Rivera, L. G. Franquelo, M. Norambuena, Model predictive control for power converters and drives: Advances and trends, IEEE Transactions on Industrial Electronics 64 (2) (2016) 935–947.

[35] S. Vazquez, J. I. Leon, L. G. Franquelo, J. Rodriguez, H. A. Young, A. Marquez, P. Zanchetta, Model predictive control: A review of its applications in power electronics, IEEE industrial electronics magazine 8 (1) (2014) 16–31.

[36] Y. Shan, J. Hu, Z. Li, J. M. Guerrero, A model predictive control for renewable energy based ac microgrids without any pid regulators, IEEE Transactions on Power Electronics 33 (11) (2018) 9122–9126.

[37] T. Dragičević, Model predictive control of power converters for robust and fast operation of ac microgrids, IEEE Transactions on Power Electronics 33 (7) (2017) 6304–6317.

[38] M. Jayachandran, G. Ravi, Decentralized model predictive hierarchical control strategy for islanded ac microgrids, Electric Power Systems Research 170 (2019) 92–100.

[39] Z. Guo, S. Li, Y. Zheng, Feedback linearization based distributed model predictive control for secondary control of islanded microgrid, Asian Journal of Control 22 (1) (2020) 460–473.

[40] Z. Yi, Y. Xu, W. Gu, Z. Fei, Distributed model predictive control based secondary frequency regulation for a microgrid with massive distributed resources, IEEE Transactions on Sustainable Energy 12 (2) (2020) 1078–1089.

[41] A. Nurkanović, A. Mešanović, A. Zanelli, G. Frison, J. Frey, S. Albrecht, M. Diehl, Real-time nonlinear model predictive control for microgrid operation, in: 2020 American Control Conference (ACC), IEEE, 2020, pp. 4989–4995.

[42] S. Batiyah, N. Zohrabi, S. Abdelwahed, R. Sharma, An mpc-based power management of a pv/battery system in an islanded dc micro-

grid, in: 2018 IEEE Transportation Electrification Conference and Expo (ITEC), IEEE, 2018, pp. 231–236.

[43] S. Batiyah, R. Sharma, S. Abdelwahed, N. Zohrabi, An mpc-based power management of standalone dc microgrid with energy storage, International Journal of Electrical Power & Energy Systems 120 (2020) 105949.

[44] Siemens PTI, PSS®e 34.2.0 model library, Siemens Power Technologies International, Schenectady, NY (2017).

[45] J. D. Ford, L. W. Ford, A. D'Amelio, Resistance to change: The rest of the story, Academy of Management Review 33 (2) (2008) 362–377. doi:10.5465/amr.2008.31193235.

[46] M. de Castro, D. Winkler, G. Laera, L. Vanfretti, S. A. Dorado-Rojas, T. Rabuzin, B. Mukherjee, M. Navarro, Version [openipsl 2.0. 0]-[itesla power systems library (ipsl): A modelica library for phasor time-domain simulations], SoftwareX 21 (2023) 101277.

[47] M.Baudette, *et al*, OpenIPSL: Open-instance power system library—update 1.5 to "iTesla power systems library (iPSL): A modelica library for phasor time-domain simulations", SoftwareX 7 (2018) 34–36.

[48] A. Bemporad, M. Morari, N. L. Ricker, Model predictive control toolbox, User's Guide, Version 2 (2004).

[49] A. Bemporad, M. Morari, N. L. Ricker, Model predictive control toolbox user's guide, The mathworks (2010).

[50] IEEE Guide for Design, Operation, and Integration of Distributed Resource Island Systems with Electric Power Systems, IEEE Std 1547.4-2011 (2011) 1–54doi:10.1109/IEEESTD.2011.5960751.

[51] B. Standard, et al., Voltage characteristics of electricity supplied by public distribution networks, BS EN (2007).

[52] D. Walker, IEEE screening guide for planned steady-state switching operations to minimize harmful effects on steam turbine-generators, IEEE Transactions on Power Apparatus and Systems 99 (4) (1980).

[53] P. Fritzson, V. Engelson, Modelica: A unified object-oriented language for system modeling and simulation, in: ECOOP, Vol. 98, Citeseer, 1998, pp. 67–90.

[54] P. Fritzson, Principles of object-oriented modeling and simulation with Modelica 3.3: a cyber-physical approach, John Wiley & Sons, 2014.

[55] F. Milano, Power system modelling and scripting, Springer Science & Business Media, 2010.

[56] F. Fachini, L. Vanfretti, M. De Castro, T. Bogodorova, G. Laere, Modeling and validation of renewable energy sources in the openipsl modelica library, in: IECON 2021–47th Annual Conference of the IEEE Industrial Electronics Society, IEEE, 2021, pp. 1–6.

[57] Homer, How Homer Calculates the PV Array Power Output (December 2023).
URL https://support.ul-renewables.com/homer-manuals-pro/how_homer_calculates_the_pv_array_power_output.html

[58] WREM Task Force, WECC battery storage dynamic modeling guideline, Western Electricity Coordinating Council, Tech. Rep (2016).

[59] WECC Renewable Energy Modeling Task Force, Solar photovoltaic power plant modeling and validation guideline (2019).

[60] C. A. Smith, A. B. Corripio, Principles and practices of automatic process control, John wiley & sons, 2005.

[61] M. Baur, M. Otter, B. Thiele, Modelica libraries for linear control systems, in: Proceedings 7th Modelica Conference, no. DOI: 1, 2009, pp. 593–602.

[62] D. Brück, H. Elmqvist, S. E. Mattsson, H. Olsson, Dymola for multi-engineering modeling and simulation, in: Proceedings of modelica, Vol. 2002, Citeseer, 2002.

[63] T. Samad, A survey on industry impact and challenges thereof [technical activities], IEEE Control Systems Magazine 37 (1) (2017) 17–18. doi:10.1109/MCS.2016.2621438.

[64] E. F. Camacho, C. B. Alba, Model predictive control, Springer science & business media, 2013.

[65] A. Baggini, Handbook of power quality, John Wiley & Sons, 2008.

[66] R. Fletcher, A general quadratic programming algorithm, IMA Journal of Applied Mathematics 7 (1) (1971) 76–91.

[67] C. Schmid, L. Biegler, Quadratic programming methods for reduced hessian sqp, Computers Chemical Engineering 18 (9) (1994) 817–832, an International Journal of Computer Applications in Chemical Engineering. doi:https://doi.org/10.1016/0098-1354(94)E0001-4.

URL https://www.sciencedirect.com/science/article/pii/0098135494E00014

[68] PDF Documentation for Control System Toolbox (January 2024).
URL https://www.mathworks.com/help/pdf_doc/control/index.html

[69] B. Southallzy, B. Buxtony, J. Marchant, Controllability and observability: Tools for kalman filter design, in: British Machine Vision Conference, Vol. 98, 1998, pp. 164–173.

[70] F. Fachini, S. Bhattacharjee, M. Aguilera, L. Vanfretti, G. Laera, T. Bogodorova, A. Moftakhari, M. Huylo, A. Novoselac, Exploiting modelica and the openipsl for university campus microgrid model development (2023) 285–292.

[71] MATLAB (December 2023). [link].
URL https://www.mathworks.com/help/mpc/

[72] Woodward product manuals - power generation controls.
URL https://wss.woodward.com/manuals/PGC/Forms/AllItems.aspx

[73] J. Marcos, L. Marroyo, E. Lorenzo, D. Alvira, E. Izco, Power output fluctuations in large scale pv plants: one year observations with one second resolution and a derived analytic model, Progress in Photovoltaics: Research and Applications 19 (2) (2011) 218–227.

[74] IEEE Standard for the Specification of Microgrid Controllers, IEEE Standard 2030.7, 2018.

[75] B. Mukherjee, L. Vanfretti, Modeling of pmu-based islanded operation controls for power distribution networks using modelica and openipsl, in: Proc. Am. Modelica Conf., 2018, pp. 9–10.

[76] D. Shi, R. Sharma, L. Yusheng, Synchronization control for reconnecting microgrid to main grid after islanding (Accessed: Feb. 28, 2024.).
URL https://patentimages.storage.googleapis.com/46/39/32/5eb66dd2b8578a/US9720395.pdf

[77] F. Fachini, A. Pigott, G. Laera, T. Bogodorova, L. Vanfretti, K. Baker, Developing a campus microgrid model utilizing modelica and the OpenIPSL library, in: 11th Workshop on Modeling and Simulation of Cyber-Physical Energy Systems, San Antonio, Texas, USA, 2023.